Article

Interannual Variation of Landfast Ice Using Ascending and Descending Sentinel-1 Images from 2019 to 2021: A Case Study of Cambridge Bay

Yikai Zhu [1,2], Chunxia Zhou [1,2,*], Dongyu Zhu [1,2], Tao Wang [1,2] and Tengfei Zhang [3]

1   Chinese Antarctic Center of Surveying and Mapping, Wuhan University, Wuhan 430079, China
2   Key Laboratory of Polar Surveying and Mapping, MNR, Wuhan University, Wuhan 430079, China
3   School of Traffic and Transportation Engineering, Changsha University of Science and Technology, Changsha 410114, China
*   Correspondence: zhoucx@whu.edu.cn

Abstract: Landfast ice has undergone a dramatic decline in recent decades, imposing potential effects on ice travel for coastal populations, habitats for marine biota, and ice use for industries. The mapping of landfast ice deformation and the investigation of corresponding causes of changes are urgent tasks that can provide substantial data to support the maintenance of the stability of the Arctic ecosystem and the development of human activities on ice. This work aims to investigate the time-series deformation characteristics of landfast ice at multi-year scales and the corresponding influence factors. For the landfast ice deformation monitoring technique, we first combined the small baseline subset approach with ascending and descending Sentinel-1 images to obtain the line-of-sight deformations for two flight directions, and then we derived the 2D deformation fields comprising the vertical and horizontal directions for the corresponding periods by introducing a transform model. The vertical deformation results were mostly within the interval [−65, 23] cm, while the horizontal displacement was largely within the range of [−26, 78] cm. Moreover, the magnitude of deformation observed in 2019 was evidently greater than those in 2020 and 2021. In accordance with the available data, we speculate that the westerly wind and eastward-flowing ocean currents are the dominant reasons for the variation in the horizontal direction in Cambridge Bay, while the factors causing spatial differences in the vertical direction are the sea-level tilt and ice growth. For the interannual variation, the leading cause is the difference in sea-level tilt. These results can assist in predicting the future deformation of landfast ice and provide a reference for on-ice activities.

Keywords: landfast ice; 2D deformation; SBAS-InSAR; interannual variation

1. Introduction

As an integral and sensitive component of the global climate system, sea ice can regulate the exchange of fluxes and radiative transfer between air and sea; it can also alter sea-surface temperature and salinity, contributing significantly to climate and environmental change in polar regions [1,2]. Landfast ice is a type of sea ice that is attached to a shore, to the front of an ice shelf, or to the perimeter of a grounded iceberg, and it is a significant component of the local physical and ecological systems [3]. Compared with floating sea ice, landfast ice plays a more crucial role in the assessment of a climate system given its characteristics of a long ice age, greater thickness, and notable seasonal trends [3,4]. Arctic landfast ice forms a rigid interface between the sea and air in nearshore areas, effectively buffering coastal erosion due to waves and, thus, influencing the nearshore sedimentation and shoreline development [5]. Landfast ice also serves as a key habitat for marine biota and as a platform for coastal populations to live on [6]. Over the last century, the expansion of transportation and resource exploitation has triggered increased human activities and further diversification of ice use in the Arctic [7]. As global temperatures have continued to

rise since the 1970s, climatic conditions in high-altitude areas of the Arctic have dramatically changed and sea ice has been rapidly declining [8], exposing ice users to unknown risks, as well as potential hazards [9]. The continued warming of the Arctic and the accelerated melting of sea ice—particularly the remarkable reduction in the extent of landfast ice in coastal areas—have led to increased ship traffic and resource exploration [10]. Therefore, determining landfast ice deformation is particularly important for local populations and organisms to anticipate potential hazard events and provide effective early warning in real time. Awareness is growing that sea ice conditions for Arctic marine operations will be a challenge that will require considerable monitoring and advanced methods in the future. This improvement must be implemented on a large scale and a regional scale to assess environmental hazards and develop effective and timely preventive measures.

The accurate determination of the large-scale and long-term deformation of landfast ice while ensuring the immediate validity and feasibility of a method has been a challenge [11]. Observing sea ice conditions in situ is difficult due to the specificity and complexity of the terrain. Satellite remote sensing is an essential tool for detecting sea ice parameters. Optical remote sensing is always effective in investigating sea ice properties, such as the extent [12] and type classification [13], with the characteristics of large spatial coverage, high spatio-temporal resolution, and a huge accessible database. However, optical methods are ineffective in making timely measurements due to weather limitations, such as clouds and fog. By the early 1990s, synthetic aperture radar (SAR) was introduced to create a superior dataset for sea ice studies, given its advantages of performing in all weather, working on all days, higher resolution, and wider monitoring coverage [5]. Intensity information from SAR has been widely applied for sea ice classification [14] and the analysis of motion [15], thickness [16], concentration [17], roughness [18] and snow-cover extent [19–21]. However, SAR backscatter does not typically provide deformation information about landfast ice or transiently stable floating ice, as the internal motion of landfast ice is too small to be identified via change detection. The advent of the SAR interferometry (InSAR) technology has opened up the possibility of using SAR data to monitor landfast ice deformation by extracting the phase difference between two SAR images with similar imaging geometries. In this manner, topography can be retrieved if acquisitions are separated in space (nonzero perpendicular baseline), or surface movement along the line-of-sight (LOS) direction can be measured if it is separated in time (nonzero temporal baseline) [22,23]. For example, Li et al. first introduced InSAR into the detection of sea ice deformation [24]. Wang et al. combined ascending- and descending-pass images to obtain the vertical and horizontal deformations of landfast ice for a single period in the Baltic Sea [25]. The preceding studies only retrieved the LOS or a 2D deformation field for a single period. This information is evidently insufficient for characterizing the deformation of landfast ice. With the launches of the Sentinel-1A satellite in 2014 and the Sentinel-1B satellite in 2016, ascending and descending datasets that cover the same area can be utilized to derive a 2D deformation field of landfast ice over a long period. Although ascending and descending SAR data cannot be combined for interferometry, they can provide InSAR observations with different imaging geometries, and 3D surface deformation can be estimated by building a multi-source heterogeneous InSAR observation model [26,27].

The coherence of ice as a monitored object is highly susceptible to external factors, such as temperature, precipitation, and wind. The small baseline subset (SBAS) InSAR technique ensures the high coherence and reliability of the inversion results by selecting interferometric combinations with small spatio-temporal baselines that are as far as possible [26,28]. SBAS-InSAR is a specific type of multi-temporal InSAR that utilizes a small subset of images to create highly accurate results [29]. This method is ideal for areas where the availability of satellite data is limited or for monitoring large areas that would otherwise be impractical with traditional InSAR. One of the key benefits of SBAS-InSAR is its ability to detect even small changes in the Earth's surface over time. This makes it a valuable tool for monitoring the effects of natural disasters, such as earthquakes [30] and volcanic eruptions [31], as well as human-made changes, such as urban development and subsi-

dence [32]. Additionally, SBAS-InSAR can be used to monitor ground deformation and subsidence in areas where oil and gas extraction is taking place [33], which helps to ensure the safety of nearby communities and infrastructure. Another advantage of SBAS-InSAR is that it is a non-invasive technique that does not require any physical access to the area being monitored. This makes it ideal for monitoring remote or difficult-to-reach areas, such as mountainous regions. Based on this, it has a great potential to be applied in monitoring natural disasters of the cryosphere, such as ice avalanches [34] and sea ice motion [35].

The current work uses ascending and descending Sentinel-1 images and the SBAS approach to derive LOS deformation results for both modes from January to April in 2019–2021. Then, the vertical and horizontal time-series deformations can be decomposed on the basis of a transform model. Finally, the temporal and spatial deformation characteristics of the test area and the factors that affect the deformation changes are analyzed in relation to the experimental results.

2. Methods

2.1. SBAS-InSAR Data Processing

SBAS-InSAR is a powerful remote sensing technique that is used to monitor changes in the Earth's surface over time [36]. This technology combines the use of SAR images with the principle of interferometry to produce highly accurate and detailed maps of the Earth's surface [37]. The procedure of SBAS-InSAR involves several steps, as shown in the pink frame of Figure 1.

(1) Data acquisition: The first step in SBAS-InSAR processing is to acquire the necessary SAR images. This typically involves using a SAR satellite to acquire multiple images of the same area at different times. The images should be acquired from similar viewing angles to ensure the highest accuracy.

(2) Image preprocessing: Once the SAR images have been acquired, they must be preprocessed to remove any noise or errors in the data. This may include correction for atmospheric effects, radiometric calibration, and speckle filtering [38].

(3) SBAS network: The next step is to select a small subset of the SAR images to use for the SBAS-InSAR analysis. This subset should be chosen based on the spatial and temporal distribution of the images and the desired accuracy of the results.

(4) Interferogram stacks: After the small baseline subset has been selected, an interferogram can be generated by applying interferometric techniques to the subset of images. The interferogram provides information about the relative height differences between the surfaces in the two images and is used to generate the final SBAS-InSAR results.

(5) Phase unwrapping: The next step is to unwrap the phase information in the interferogram to remove any phase ambiguities. This is typically done by using algorithms such as the least-squares method or the multichannel algorithm [39].

(6) Time-series deformation inversion: A singular value decomposition (SVD) is utilized here to estimate the minimal norm least-squares solution of the average deformation rate of each period [40,41]; meanwhile, the times-series deformation can be calculated as well [42].

### 2.2. Calculation of Horizontal and Vertical Deformations

The time-series deformation results of ascending and descending orbits were derived via the SBAS method. In this work, the time-series deformation results were used in combination with the classical function model to monitor the 3D deformation of landfast ice in the study area.

The classical function model was established on the basis of the geometric relationship between the InSAR observations and 3D deformations. Figure 2 shows a schematic diagram of 3D deformations from different perspectives. In accordance with Figure 2a,b, the deformation vector along the LOS direction is located on a 2D plane composed of a ground direction (projection of the LOS direction on the horizontal plane) and a vertical direction.

The ground range and vertical direction are perpendicular to each other; thus, the following expression can be obtained according to the geometric relationship in Figure 2a [43]:

$$d_{\text{LOS}}^{\text{A}} = d_{\text{u}} \cdot \cos\theta_{\text{inc}}^{\text{A}} + d_{\text{h}} \cdot \sin\theta_{\text{inc}}^{\text{A}} \tag{1}$$

where d_{u} and d_{h} define, respectively, the vertical and ground displacement vectors; $\theta_{\text{inc}}^{\text{A}}$ represents the pixel-based incidence angle of the radar pulse signal.
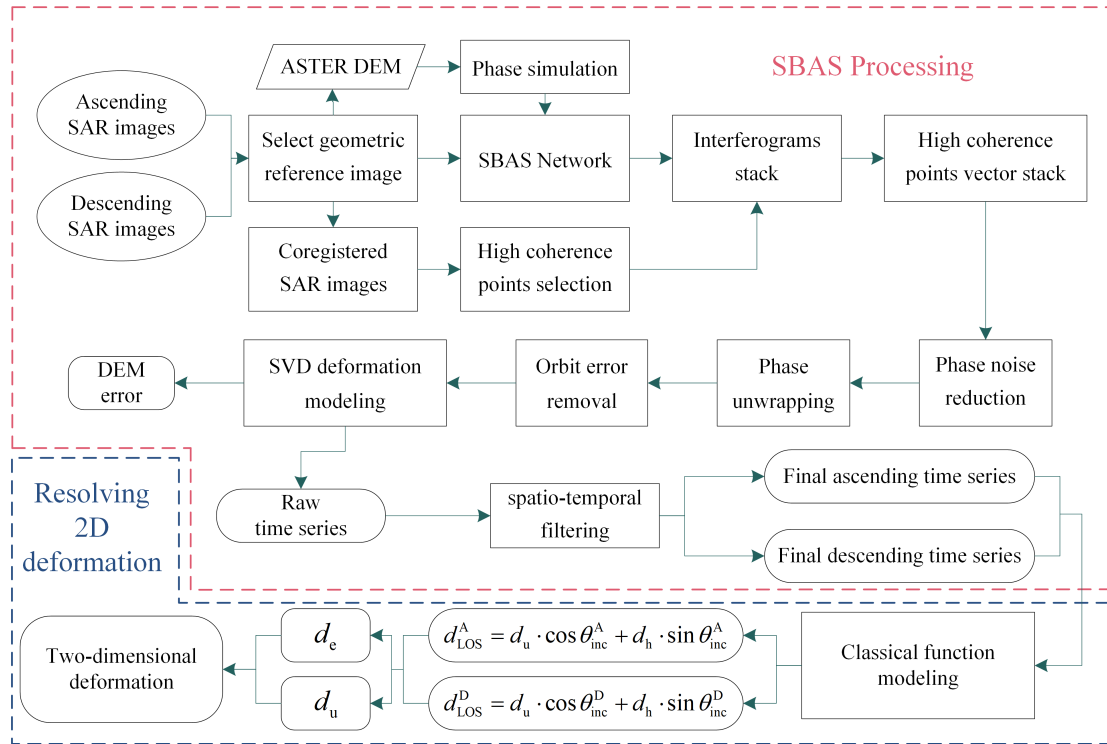
Figure 1. The workflow of the methodology is composed of two parts: SBAS processing and 2D deformation resolution.

The ground displacement vector is composed of the eastern and northern components, as illustrated in Figure 2b [30,44].

$$d_{\text{h}} = d_{\text{c}} \cdot \left[-\sin\left(\alpha_{\text{AZI}}^{\text{A}} - 3\pi/2\right) \right] + d_{\text{n}} \cdot \left[-\cos\left(\alpha_{\text{AZI}}^{\text{A}} - 3\pi/2\right) \right] \tag{2}$$

where d_{e} and d_{n} represent, respectively, the east–west and north–south displacement vectors; $\alpha_{\text{AZI}}^{\text{A}}$ is the orbit azimuth angle (positive clockwise from the north), and $\alpha_{\text{AZI}}^{\text{A}} - 3\pi/2$ actually defines the angle between the ground range direction and the north. By substituting Equation (2) into Equation (1), the relationship between the LOS deformation and the 3D surface deformation vector can be established in the case of the ascending mode.

$$
\begin{aligned}
d_{\text{ios}}^{\text{A}} = {} & - d_{\text{c}} \cdot \sin\theta_{\text{inc}}^{\text{A}} \cdot \sin\left(\alpha_{\text{AZI}}^{\text{A}} - 3\pi/2\right) \\
& - d_{\text{n}} \cdot \sin\theta_{\text{inc}}^{\text{A}} \cdot \cos\left(\alpha_{\text{AZI}}^{\text{A}} - 3\pi/2\right) + d_{\text{u}} \cdot \cos\theta_{\text{inc}}^{\text{A}}
\end{aligned}
\tag{3}
$$

Similarly, the relationship between the LOS deformation and 3D surface deformation can be constructed in the descending mode as follows [45]:

$$
\begin{aligned}
d_{\text{LOS}}^{\text{D}} = {} & - d_{\text{c}} \cdot \sin\theta_{\text{inc}}^{\text{D}} \cdot \sin\left(\alpha_{\text{AZI}}^{\text{D}} - 3\pi/2\right) \\
& - d_{\text{n}} \cdot \sin\theta_{\text{inc}}^{\text{D}} \cdot \cos\left(\alpha_{\text{AZI}}^{\text{D}} - 3\pi/2\right) + d_{\text{u}} \cdot \cos\theta_{\text{inc}}^{\text{D}}
\end{aligned}
\tag{4}
$$

Sentinel-1 is a near-polar orbit satellite with a low sensitivity in the north–south direction. Therefore, performing high-precision detection of movement in this direction is difficult. We assume that the north–south deformation of landfast ice in the study area is zero. Then, 2D deformations comprising the east–west and vertical deformations can be decomposed from the combination of ascending and descending results of the same epoch. This issue can be resolved by combining Equations (3) and (4).

$$
\begin{bmatrix} d_{\mathrm{u}} \\ d_{\mathrm{e}} \end{bmatrix} = \begin{bmatrix} \cos\theta_{\mathrm{inc}}^{\mathrm{A}} & -\sin\theta_{\mathrm{inc}}^{\mathrm{A}}\sin(\alpha_{\mathrm{AZI}}^{\mathrm{A}} - 3\pi/2) \\ \cos\theta_{\mathrm{inc}}^{\mathrm{D}} & -\sin\theta_{\mathrm{inc}}^{\mathrm{D}}\sin(\alpha_{\mathrm{AZI}}^{\mathrm{D}} - 3\pi/2) \end{bmatrix}^{-1} \begin{bmatrix} d_{\mathrm{LOS}}^{\mathrm{A}} \\ d_{\mathrm{LOS}}^{\mathrm{D}} \end{bmatrix} \tag{5}
$$
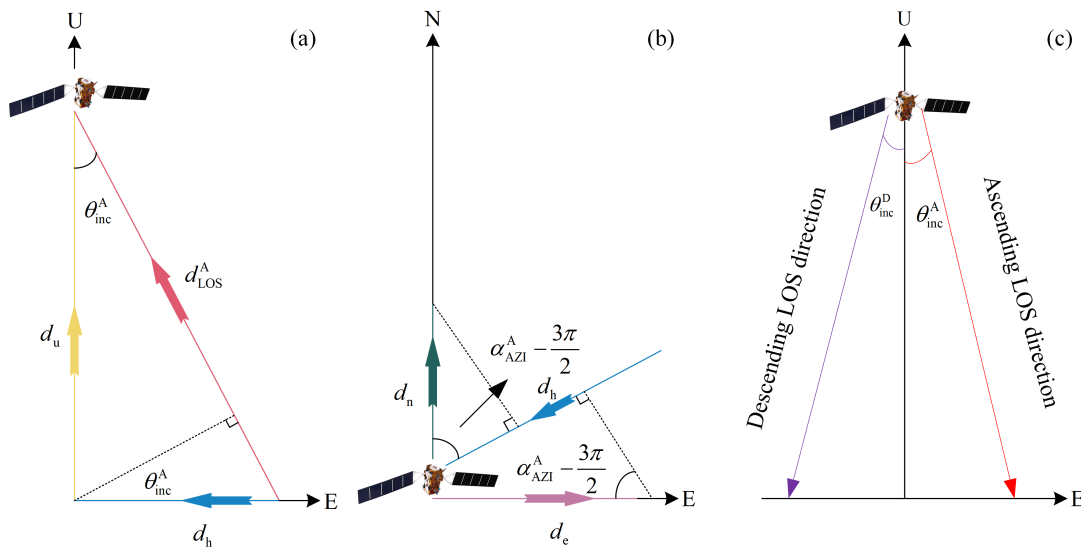
Figure 2. Geometric relationship of the LOS direction from (**a**) the horizontal perspective and (**b**) the vertical perspective in the Sentinel-1A ascending orbit mode, as well as (**c**) the imaging geometry of ascending and descending images.

3. Study Area and Datasets

3.1. Cambridge Bay

The study site was located in the southern part of Cambridge Bay, as shown in Figure 3. Cambridge Bay is a hamlet located on Victoria Island in the Kitikmeot Region in Nunavut, Canada. Given its unique geographical situation, i.e., it is located on the western end of Queen Maud Gulf, where it narrows into Dease Strait, Cambridge Bay is a transportation and administrative hub for the Kitikmeot Region and the largest stop for passenger and polar research vessels traversing the Arctic Ocean's Northwest Passage [46]. Cambridge Bay has a polar climate, that is, no month has an average temperature of 10 °C or higher. In accordance with the regional sea ice charts available from the Canadian Ice Service Data Archive (CISDA), landfast ice dominates the ice type, with various thickness values at different dates during the winter [47].
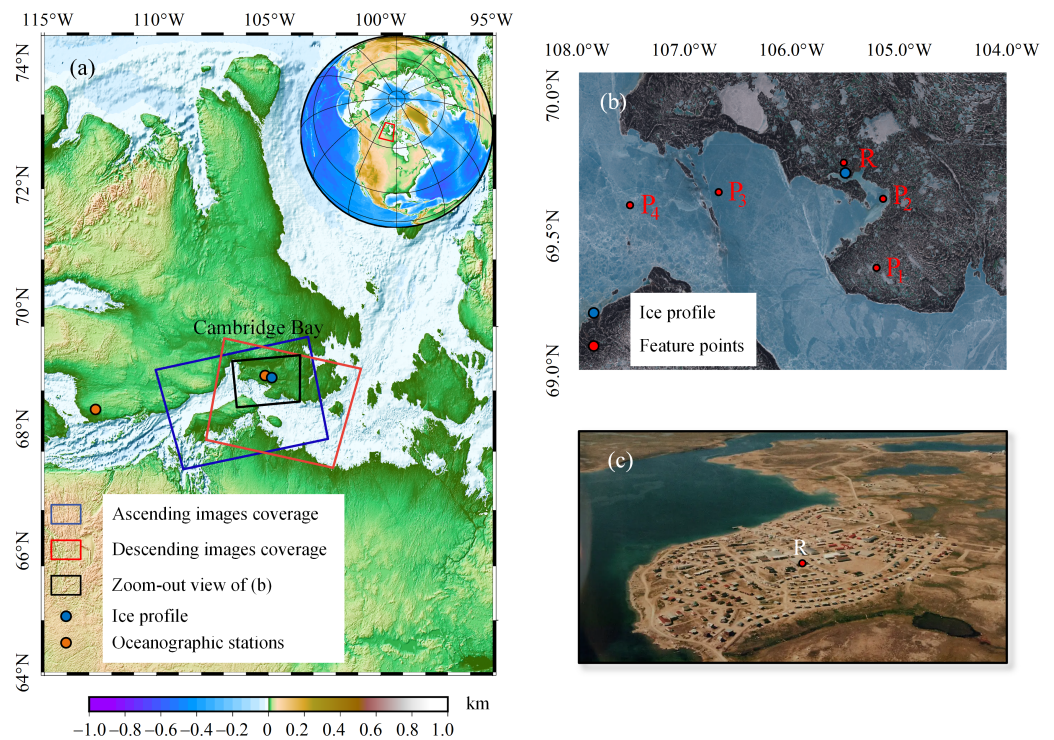
Figure 3. Study area: (**a**) Location of Cambridge Bay, with the blue and red rectangles representing, respectively, the coverage of ascending and descending images; the black rectangle defines the zoomed-out view of (**b**); the yellow circles and blue circle represent the oceanographic stations and ice profile. (**b**) Specific location of feature and reference points of phase unwrapping, with the Sentinel-2 images being the base map. (**c**) Site picture of Cambridge Bay where reference point R is located.

3.2. Sentinel-1 Images and Reference Data

The Sentinel-1 mission comprises a constellation of two polar-orbiting satellites (Sentinel-1A and Sentinel-1B, which share the same orbital plane) that operate day and night to perform C-band SAR imaging, thus enabling them to offer reliable and repeated wide-area monitoring regardless of the weather [48]. To investigate the interannual deformation characteristics of landfast ice in the area of interest, the three-year (2019–2021) Sentinel-1 single-look complex (SLC) products over Cambridge Bay were used to retrieve the 2D deformation results (the specific characteristics are listed in Table 1). Considering the coherence level of the observed objects, SAR images from January to April in each year were selected for the experiments to avoid the incoherence caused by ice melting. The interferometric processing was accomplished with the GAMMA software, which included interferometry and phase unwrapping. In the process of SBAS-InSAR processing, the master image of each subset was connected to the two slave images whose acquisition dates were the closest to that of the master (Figure A1) to minimize the probability of temporal decoherence and obtain ideal interferometric and unwrapping results. The coherence threshold of 0.3 was adopted to ensure relatively reliable high-quality point selection. The multi-look ratio was set to 10:2 in this work. In addition, a Goldstein filter was used to suppress the noise phase, and the commonly used minimum cost flow algorithm was applied for phase unwrapping. The reference point R of phase unwrapping was located in the residential area of Cambridge Bay, which was regarded as stable (Figure 3).

The temperature, tide, and wind of two weather stations (Austin Bay and Cambridge Bay, the locations of which are shown in Figure 3) were collected from the official website of the Government of Canada to understand the ice conditions and interpret the deformation characteristics in Cambridge Bay. Moreover, the ice draft data available from the Ocean Networks Canada Data Archive were downloaded and are displayed in Figure 4.

Table 1. Characteristics of the Sentinel-1 images used in this work.

Flight Direction	Beam Mode	Polarization	Incidence Angles (°)	Repeat Cycle (Days)	Number of Scenes Acquired
Ascending	IW	VV	38.98	12	28
Descending	IW	HH	39.15	12	29
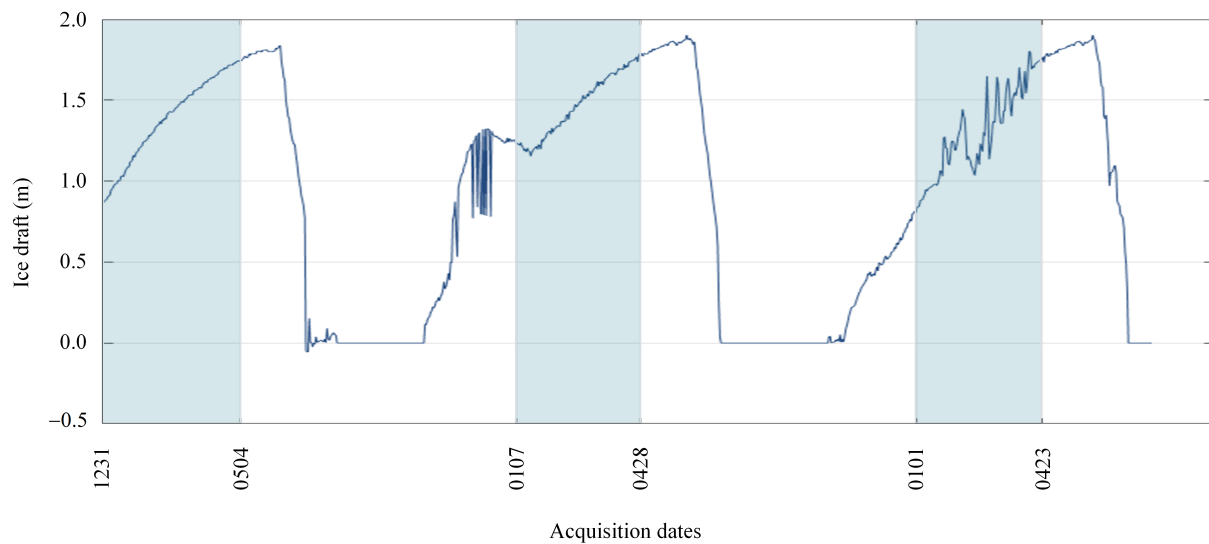
Figure 4. Ice draft changes from an ice profiler near Cambridge Bay. The part with a light-blue background is the period that covers the acquisition dates of the SAR images used in this work.

4. Results

4.1. Average Coherence and Interferograms

Coherence in InSAR is defined as the cross-correlation coefficient in the registration of two SLCs [49]. It is a widely used byproduct of InSAR [50,51]. It is also a significant indicator that is generally used to evaluate the quality of the interferometric phase. A higher coherence can effectively alleviate the problem of phase discontinuity, which introduces errors in the follow-up steps, yielding a more reliable displacement result. In the current work, the average coherence from C-band Sentinel-1 InSAR pairs was counted and is displayed in Figure A2 for the period of January–April 2019–2021. The majority of average coherence values were within the range of [0.3, 0.4]. The coherence level of landfast ice in the present work was evidently lower than those of traditional research objects, such as roads, bridges, mining areas, and earthquakes [52,53]. The factors for decorrelation could mostly be attributed to the physical properties of the ice, which was susceptible to temperature, wind, and precipitation. In addition, the ice growth exhibited the potential to decrease coherence by increasing freeboard, and the internal random motion (e.g., the dynamics of brine inclusions) of ice and snow could also lower it [22].

From Equation (5), we acquired two interferogram subsets (ascending and descending) for each year during the period of 2019–2021. Given the form of the fringes, they were unlikely to be caused solely by the displacement on the surface snow layer or ice growth. Instead, the inducer was likely to be a mechanical metamorphosis. We chose a representative selection of filtered interferograms from each subset for presentation (Figure A3). Each color-cycle change indicates that the deformation change along the LOS direction is half of a wavelength in length. Dense interferometric fringes correspond to a large phase gradient. Rather, a sparse fringe distribution indicates that the region remained relatively stable. As a general rule, horizontal movement dominated the surface deformation when the fringes exhibit an evident parallel trend, while circular fringes indicate that vertical deformation played a major role [54]. From the spatial distribution shown in Figure A3, sparse suborbicular fringes were distributed near Cambridge Bay, while the quantity of fringes gradually increased with increasing distance from land, and the fringes were arranged in parallel.

This finding suggests that landfast ice closer to the shore was more stable under the effect of a buttressing force. In terms of time-series variation, high-density interferometric fringes were spread across the study area in January and February. With the passing of time, the quantity and shape of fringes changed markedly from March to April, with mostly sparse circular fringes, indicating that the deformation in this area was relatively significant from January to February, and the landfast ice gradually became stable from March to April, with enhanced interference immunity. Some fringe discontinuities could be observed in these interferograms; these were largely due to the influence of ice ridges on the ice roads caused by anthropogenic activities during winter. In addition, four feature points (P_1, P_2, P_3, and P_4) were marked for a better exploration of the deformation evolution pattern in this region. The concrete positions of these points are shown in Figure 3. P_1 is located on land, with the primary use of checking the reliability of the experimental results. P_2 is close to Cambridge Bay, where interferometric fringes are sparse and the magnitude of movement is relatively small. P_3 is located near the ice ridge. It can be used to investigate the deformation characteristics of landfast ice with support from external forces. P_4 is located on smooth landfast ice without the interference of visible factors. Numerous dense fringes are distributed near P_4, indicating the existence of a large deformation.

4.2. Ascending and Descending LOS Deformations

As described in Section 2.1, the SBAS method was used to derive the time-series deformation from 2019 to 2011 on the basis of ascending and descending Sentinel-1 images. All InSAR measurements were calibrated as changes relative to a reference point, which is labeled with R in Figure 3. The corresponding LOS deformation results from the ascending and descending datasets are displayed in Figures A4–A9. A positive or negative sign represents movement closer to or away from the SAR sensor. In terms of the overall spatial distribution, the results for the ascending and descending modes reflected nearly opposite deformation trends, with a maximum accumulated movement of −52 cm for ascending images and 55 cm for descending images. The different geometries and polarizations (HH was used in the ascending mode, while VV was used in the descending mode) adopted in the deformation monitoring contributed to the discrepancies in the results of the ascending and descending images. The same deformation may exhibit the opposite direction to that of a deformation monitored under the opposite geometry. The time-series deformation results of the four feature points located in the different areas mentioned in Section 4.1 were extracted to further reveal the generated deformation characteristics, as shown in Figure 5. P_1 and P_2 remained relatively stable in terms of temporal variation, which was closely related to their geographical locations. P_1 was located on land, and point P_2 was close to Cambridge Bay. By contrast, the remaining two feature points had significantly larger deformation magnitudes and exhibited opposite deformation directions for the different datasets. P_3 experienced a downward displacement along the LOS direction at a total of −4.7 cm, −7 cm, and −9.6 cm from 2019 to 2021 with ascending images, and it presented the opposite trend at 21 cm, 15 cm, and 20 cm from 2019 to 2021 under the descending geometry. The deformation trend of P_4 was similar to that of P_3, and they only differed in magnitude.
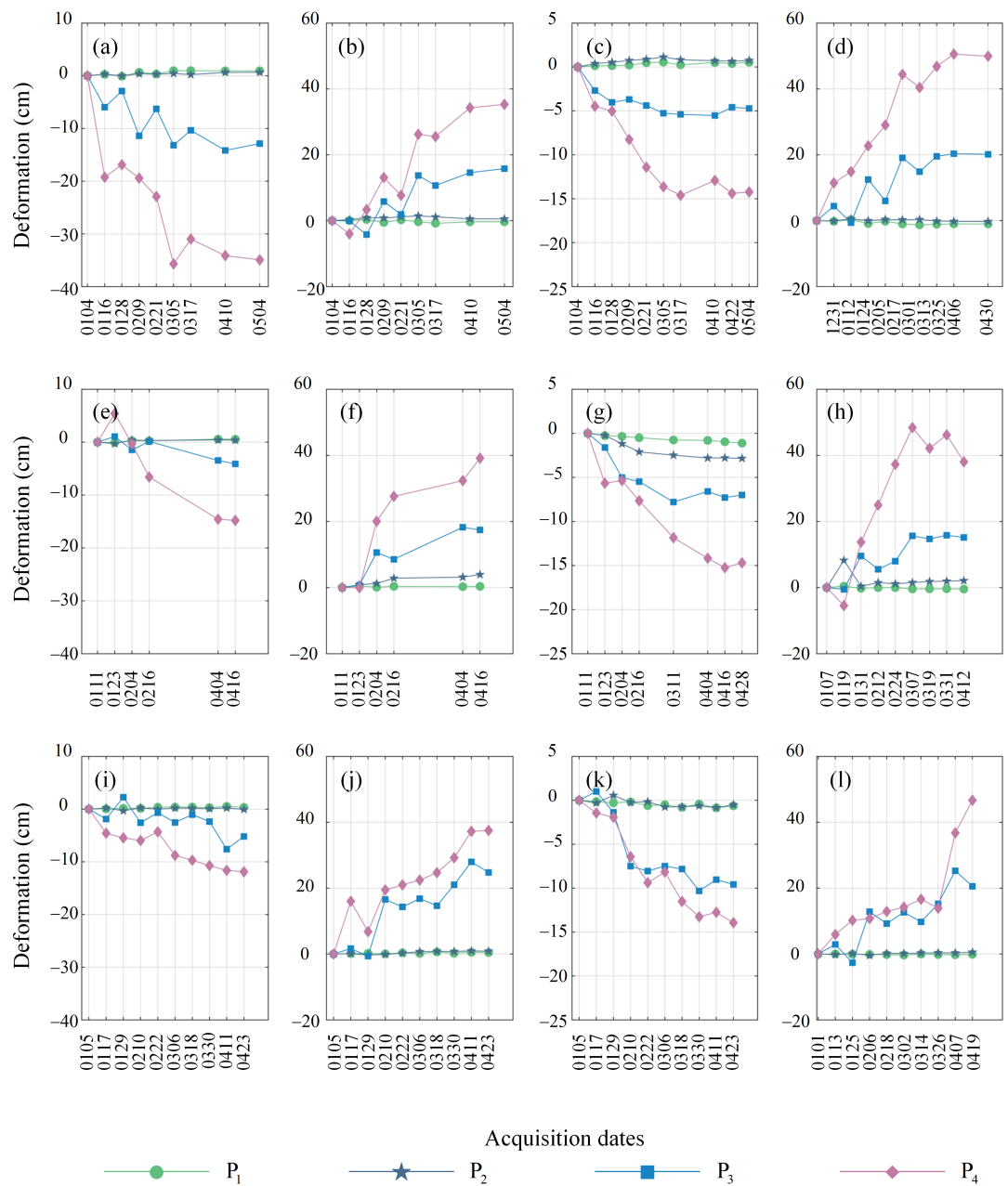
Figure 5. Cumulative deformation from different directions of each feature point: (**a**) vertical deformation in 2019; (**b**) horizontal deformation in 2019; (**c**) ascending LOS deformation in 2019; (**d**) descending LOS deformation in 2019; (**e**) vertical deformation in 2020; (**f**) horizontal deformation in 2020; (**g**) ascending LOS deformation in 2020; (**h**) descending LOS deformation in 2020,; (**i**) vertical deformation in 2021; (**j**) horizontal deformation in 2021; (**k**) ascending LOS deformation in 2021; (**l**) descending LOS deformation in 2021.

4.3. Horizontal and Vertical Deformations

The temporal coverage of the Sentinel-1 ascending images was not completely consistent with that of the descending images. The 2D time-series deformation results could only cover overlapping periods. The horizontal time-series displacement maps from 2019 to 2021 are displayed in Figures 6–8, and the vertical deformation results are presented in Figures 9–11. A positive or negative sign indicates that the movement was uplifted (or moved to the east) or sunk (or moved to the west). A vertical deformation within the range of [−68, 23] cm and a horizontal deformation within the range of [−26, 78] cm were derived in 2019. Meanwhile, the magnitude of vertical deformation in 2020 and 2021 was apparently lower, i.e., within the range of [−45, 12] cm. In summary, the movement of the coastal zone tended towards zero in both directions, and it was evidently smaller than that of the channel. The results showed a predominant subsidence on the western side, with an overall tendency for landfast ice to migrate eastwards. In terms of the time sequence, the period with a large deformation rate occurred mostly from early January to early March. Thereafter, the deformation rate in the study area significantly decreased. As for the horizontal deformation, the landfast ice retained similar variation characteristics from 2019 to 2021, within the range of [−26, 78] cm. Most areas showed a trend of eastward movement, especially in the western flank.

The time-series deformation results of the feature points mentioned above were extracted and are displayed in the first and second columns of Figure 5 and Table 2. In 2019, P_1, P_2, P_3, and P_4 experienced settlement at 0.1 cm, 0.6 cm, 12.8 cm, and 34.9 cm, respectively. P_1, P_2, P_3, and P_4 experienced eastward movement at 0.1 cm, 0.5 cm, 15.8 cm, and 35.3 cm, respectively. Similarly, the magnitude of vertical deformation in 2019 was greater than those in the other two years. In 2020, the cumulative maximum deformations of P_1, P_2, P_3, and P_4 were 0.1 cm, −0.3 cm, −4.1 cm, and −14.8 cm, respectively, in the vertical direction and 0.1 cm, 0.4 cm, 17.4 cm, and 39.1 cm, respectively, in the horizontal direction. In 2021, the cumulative maximum deformations of P_1, P_2, P_3, and P_4 were 0 cm, −0.3 cm, −7.6 cm, and −11.9 cm, respectively, in the vertical direction and 0.03 cm, 0.4 cm, 24.7 cm, and 37.5 cm, respectively, in the horizontal direction.

Table 2. Accumulated deformation along the vertical and horizontal directions from 2019 to 2021 (in cm).

| Feature Points	Years (Movement Direction)					
	2019 (Vertical)	2019 (Horizontal)	2020 (Vertical)	2020 (Horizontal)	2021 (Vertical)	2021 (Horizontal)
P_1	−0.1	0.1	0.1	0.1	0	0
P_2	−0.6	0.5	−0.3	0.4	−0.3	0.4
P_3	−12.8	15.8	−4.1	17.4	−7.6	24.7
P_4	−34.9	35.3	−14.8	39.1	−11.9	37.5

The factors that affected the deformation characteristics will be discussed in Section 5. In addition, SAR images obtained at different times were slightly different under different SAR conditions, such as the atmospheric conditions and polarization [55]. This phenomenon led to changes in intensity, coherence, and measurement in the InSAR analysis, and these are not evaluated in the current work.
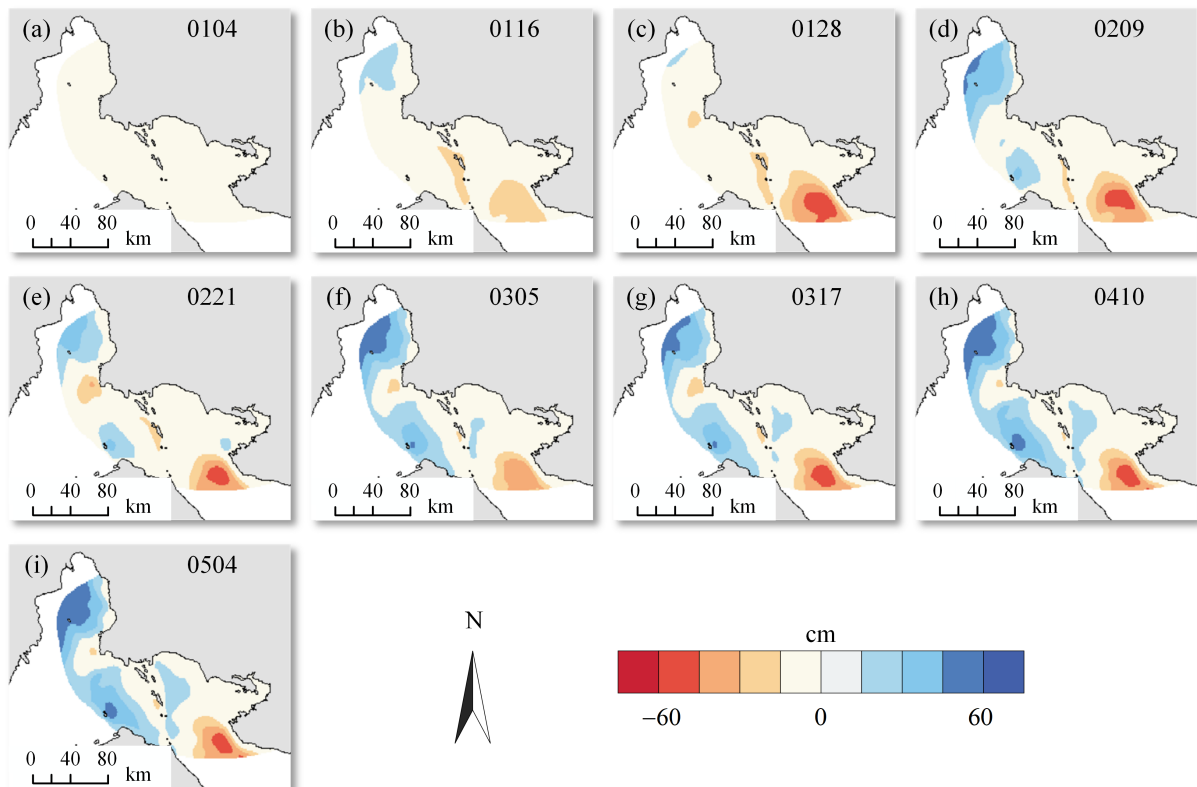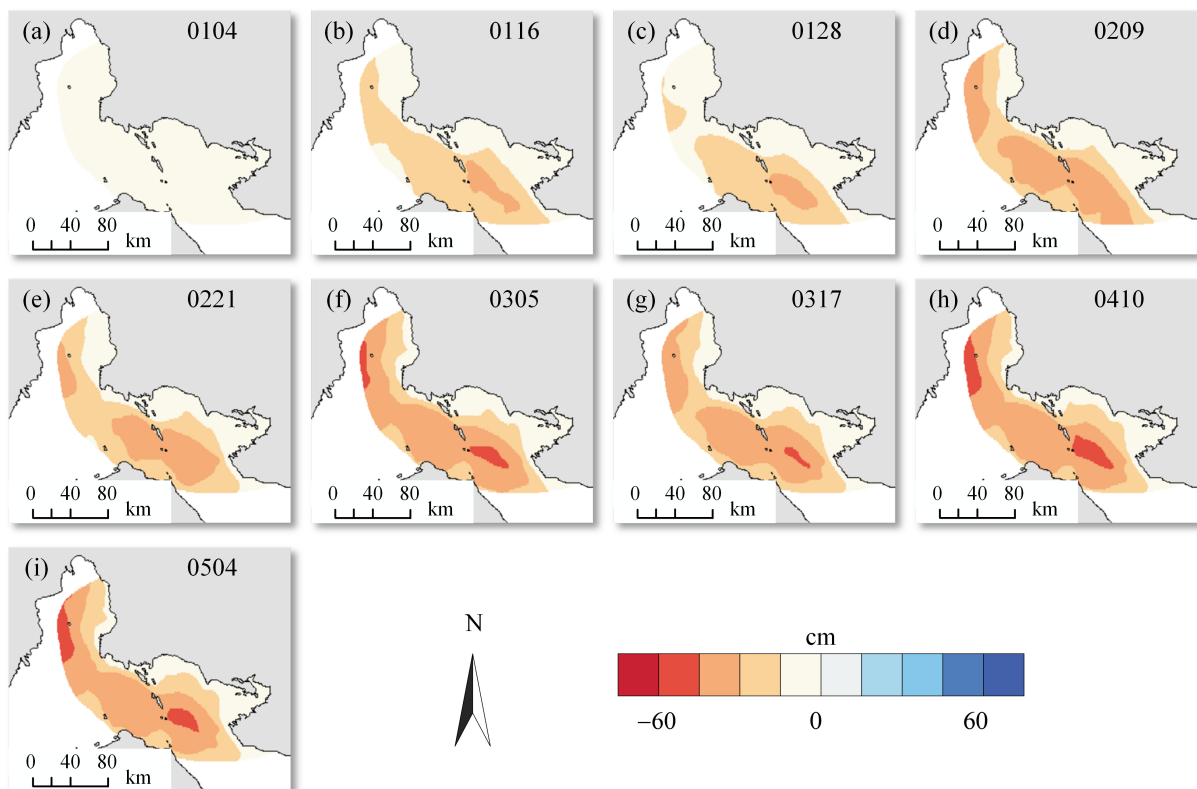
Figure 6. Retrieved time-series horizontal deformation from January 2019 to May 2019: the top-right number of subfigures (**a–i**) represents the corresponding SAR images acquisition dates.
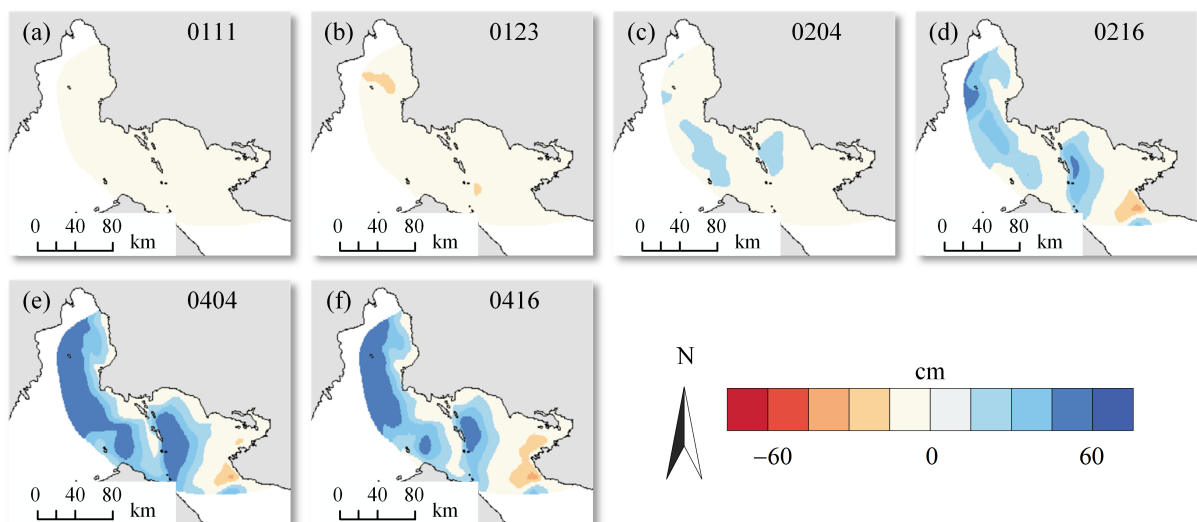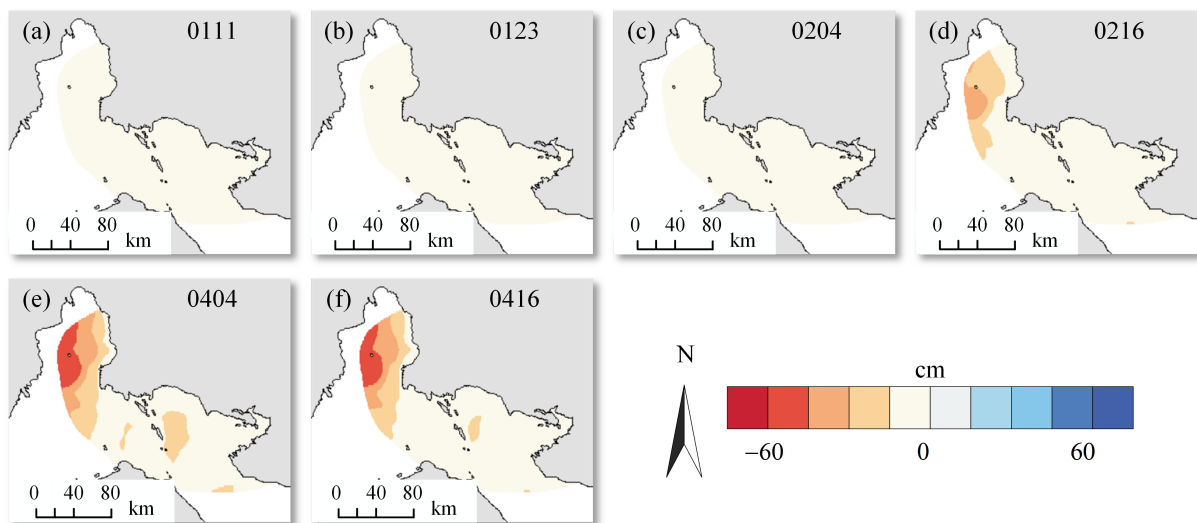

Figure 7. Retrieved time-series horizontal deformation from January 2020 to April 2020: the top-right number of subfigures (**a–f**) represents the corresponding SAR images acquisition dates.
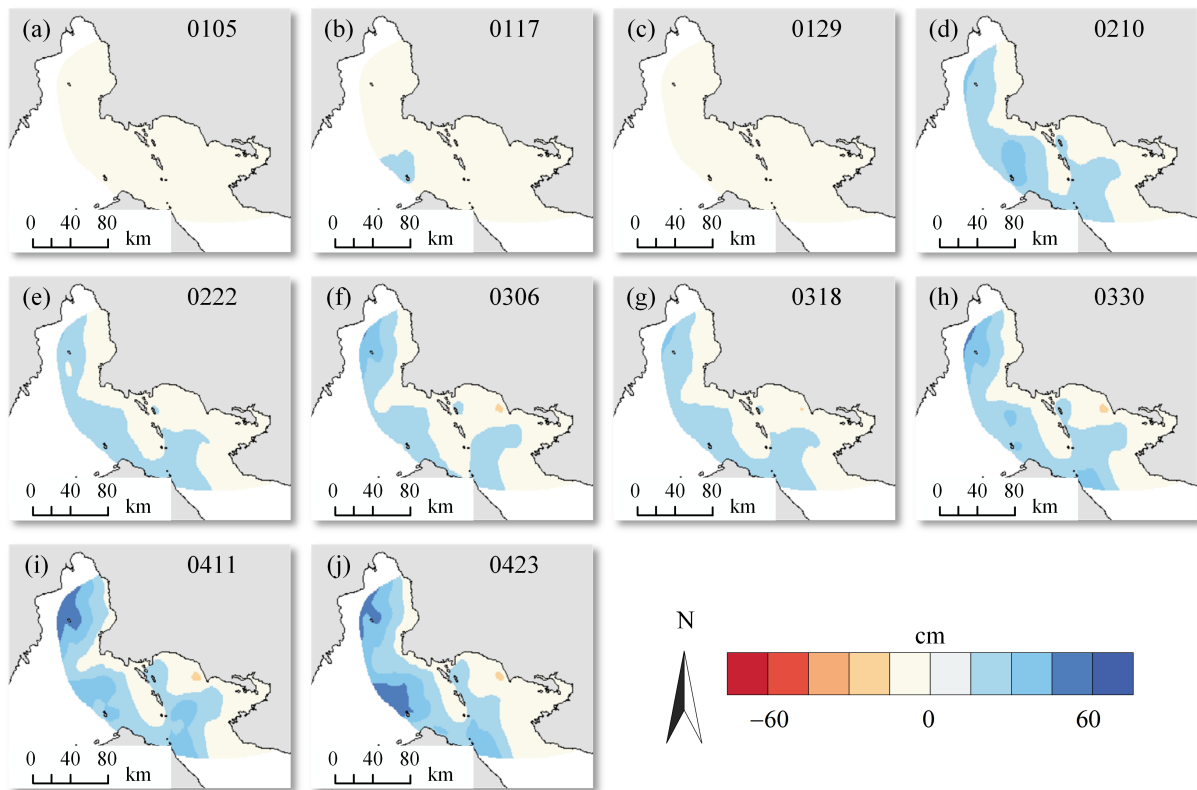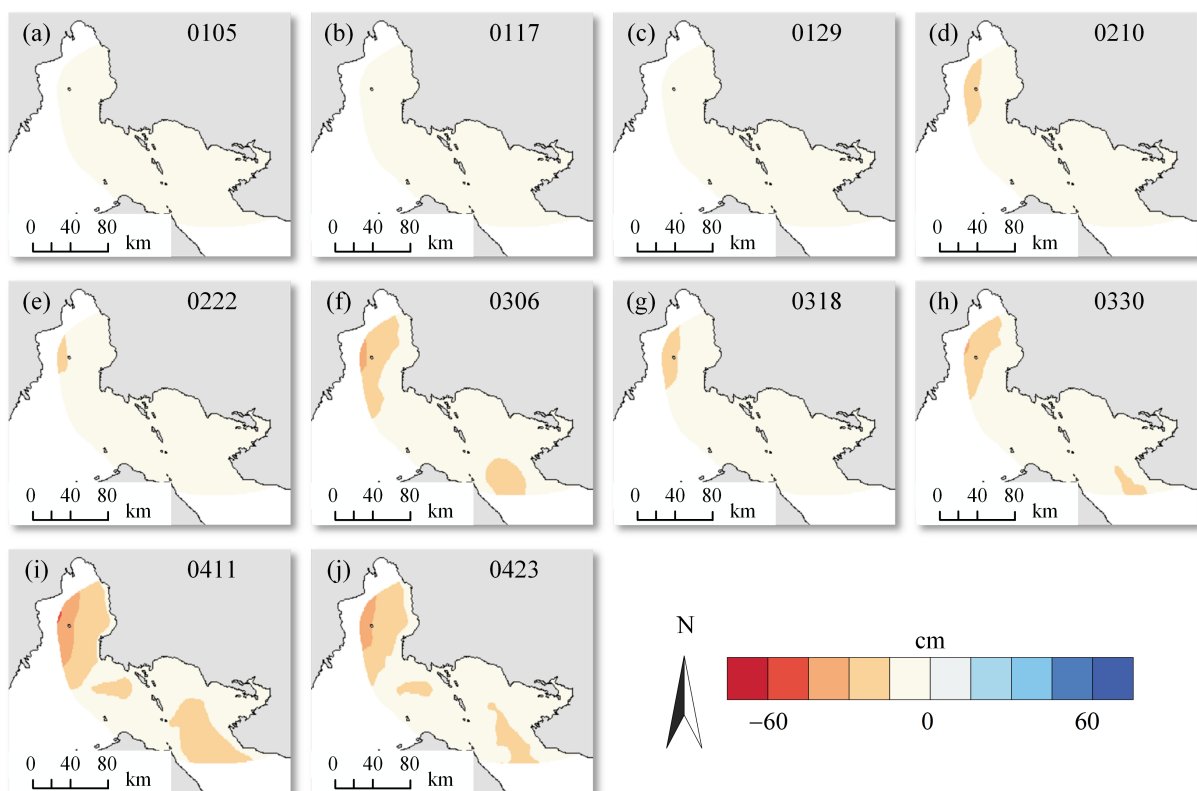
Figure 8. Retrieved time-series horizontal deformation from January 2021 to April 2021: the top-right number of subfigures (**a**–**j**) represents the corresponding SAR images acquisition dates.

Figure 9. Retrieved time-series vertical deformation from January 2019 to May 2019: the top-right number of subfigures (**a**–**i**) represents the corresponding SAR images acquisition dates.

Figure 10. Retrieved time-series vertical deformation from January 2020 to April 2020: the top-right number of subfigures (**a**–**f**) represents the corresponding SAR images acquisition dates.

Figure 11. Retrieved time-series vertical deformation from January 2021 to April 2021: the top-right number of subfigures (**a**–**j**) represents the corresponding SAR images acquisition dates.

4.4. Validation

To compensate for the unavailability of external validation data over Cambridge Bay, the residual phase of each interferogram was calculated and selected as the accuracy index. In addition, we also compared the results of this work with those of similar published studies to verify the reliability of the experimental results.

The residual phase can be estimated by subtracting the low-pass deformation phase from the unwrapped phase, and this has the ability to evaluate the accuracy of deformation modeling in InSAR analysis [56]. A smaller residual phase indicates a higher accuracy of

deformation inversion. The average residual phase for each subset of SBAS processing is provided in Table 3. Its value was less than 1 rad in any flight direction and acquisition year, demonstrating that the conventional linear model used in the SBAS method was sufficiently accurate for deformation estimation in the current work.

Table 3. Average residual phases of different flight directions from 2019 to 2021 (in rad).

Flight Direction	Year		
	2019	**2020**	**2021**
Ascending	0.85	0.67	0.75
Descending	0.68	0.71	0.81

To our knowledge, few cases have used InSAR techniques—particularly multi-temporal InSAR—to monitor landfast ice deformation. Marbouti et al. first explored Sentinel-1 images with the DInSAR technology to retrieve deformations in 2015; a deformation of landfast ice on the order of 40 cm was observed in the Baltic Sea [57]. Only a single period of LOS deformation was obtained here due to the paucity of data, thus failing to recover the true 3D deformation field. Wang et al. combined ascending and descending data to retrieve the vertical and horizontal deformations of landfast ice in the Baltic Sea [25]. They extended the dimensionality of InSAR technology to landfast ice deformation monitoring. For long-term monitoring, Chen et al. utilized the multi-dimensional SBAS method to process time-series observations for retrieving 2D deformations that comprised the vertical and horizontal directions in Cambridge Bay [58]. At present, only Chen et al. has applied multi-temporal InSAR to the monitoring of landfast ice deformation in Cambridge Bay. However, they only investigated deformation characteristics for 1 year and did not systematically address the potential causes of deformation. In the current work, ascending and descending datasets were used to detect the time-series 2D deformation for 3 years (2019–2021), and the possible causes of deformation are summarized and discussed in a later section. Given the lack of external in situ measurements, we compared the results retrieved for the same geographical location with those of previous studies to verify the accuracy and improvements of the time-series 2D deformation in this work. The deformation results for the same acquisition period (2019) are listed in Table 4. A small deformation difference indicates that the two results maintained a high level of agreement, thus proving the reliability and authenticity of the experimental results in the current work.

Table 4. Comparison of deformation results (in cm).

Deformation Results	LOS		2D	
	Ascending	**Descending**	**Vertical**	**Horizontal**
Study of Chen et al.	−13.6	16.7	9.4	21.7
Results in the current work	−14.6	19.0	5.7	23.2
Deformation difference	1.0	−2.3	2.7	−1.5

5. Discussion

5.1. Suggested Reasons for Deformation

In this work, 2D deformation results that included the east–west and vertical displacements of landfast ice in Cambridge Bay from January to April in 2019–2021 were obtained by combining ascending and descending images. The suggested reasons for the deformations are described from two perspectives. The factors that affect horizontal deformations include ocean currents, winds, and thermal expansion [25]. Meanwhile, the factors that affect vertical deformation include temperature, ice growth, and sea-level tilt [58], which are further described below.

The horizontal deformation of the landfast ice presented an eastward migration trend, except for landfast ice around the coastal area, which remained relatively stable. The cold ocean current from Beaufort Sea flows through Amundsen Gulf, Coronation Gulf, and Cambridge Bay from west to east [59], indicating the west-to-east current direction in this area. Thus, the cold ocean current possesses the ability to promote the eastward movement of landfast ice near Cambridge Bay in the horizontal direction. For the winds, their direction and magnitude exerted a certain degree of influence on the horizontal deformation. Figure 12 shows the wind information of the corresponding research period (2019–2021), including the speed and direction. Overall, the study area was dominated by westerly winds. The continuous winds from the west caused ice floes to drift eastward and compress the western boundary of the landfast ice, resulting in an eastward movement. Simultaneous dilatation was observed along the western boundary, which typically occurs under such forcing conditions [60]. In particular, the largest horizontal displacement rate for P_3 occurred between 4 January 2019 and 5 March 2019, with an accumulative deformation of 14 cm. As shown in Figure 12, the wind direction remained unchanged, while the speed rose from 17 km/h to 27 km/h, indicating an enhanced wind force. The combined actions of the wind speed and direction caused the most severe horizontal movement in this period.

Ice draft data collected from an ice profiler are shown in Figure 4. Ice growth began in late October every year and consistently maintained an upward trend, exhibiting some fluctuations before reaching the maximum value of approximately 1.8 m in the middle of or in late May. In general, a 9:1 proportional relationship existed between the ice draft and freeboard [61], that is, the thickness of the freeboard would increase by approximately 20 cm when the increment in the ice draft reaches 1.8 m. This assumption was inconsistent with the deformation magnitude observed in the current work. Therefore, except for the growth of ice, variations in sea level should be taken into account with regard to the vertical movement of landfast ice. Absolute sea-level changes cannot be reflected in an interferogram, as landfast ice is afloat, but sea-level tilt affects the distribution of vertical movement. Fringes can be affected by sea-level variation in accordance with $\Delta R = \varphi/2k$, where φ defines the interferometric phase, and $k = 2\pi/\lambda$ represents the wave number [62]. Horizontal movements could be estimated through the placement of oceanographic stations. Two oceanographic stations, Austin Bay and Cambridge Bay, could provide the required tidal data with a sampling frequency of 1 h. The corresponding spatial distribution of vertical deformation could be derived by measuring the differences in sea-level changes between the two meteorological stations during the same period. For example, the sea level in Austin fell from 18 cm to 8 cm from 31 December 2018 to 22 April 2019, whereas in Cambridge Bay, a reduction from 46 cm to 45 cm was observed. Therefore, the maximum relative change in the water level was 9 cm. According to the statistical results presented in Figure 13, the relative sea-level variation amplitude in the Austin area was higher than that in Cambridge Bay during most periods, leading to a phenomenon in which the settlement magnitude in the west was greater than that in the east. This phenomenon was consistent with the spatial distribution of the vertical deformation.
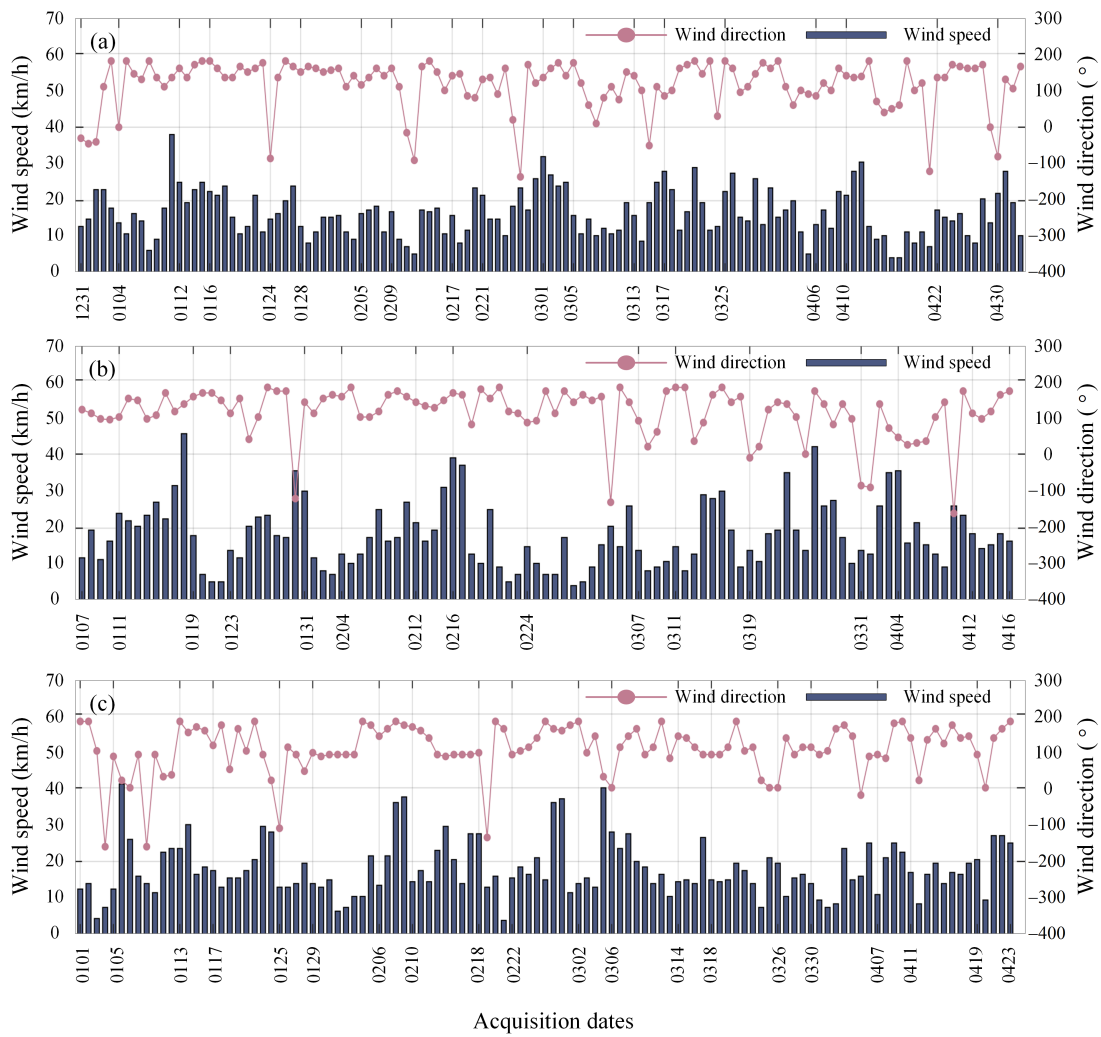
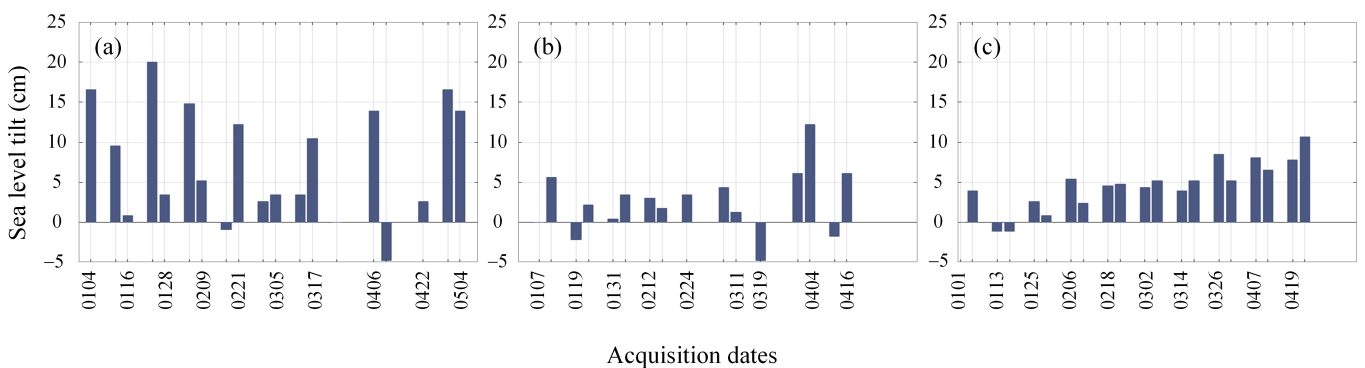**Figure 12.** Collected wind data, including direction and speed, in (**a**) 2019, (**b**) 2020, and (**c**) 2021.

Figure 13. Sea-level tilt between Cambridge Bay and Austin Bay: (**a**) 2019, (**b**) 2020, and (**c**) 2021.

5.2. Possible Causes of Interannual Variation

In accordance with the interannual experimental results, the variability of landfast ice in the study area tended to be stable. The magnitude of deformation in 2019 was significantly higher than those of the other two years. By collating and analyzing the external data, we determined that the three-year average temperatures during the period covered by the SAR images were −27.4 °C, −28.4 °C, and −27.6 °C, with slight variations. Meanwhile, the maximum temperature was considerably below 0 °C. The possibility that melting caused the severe deformation of the ice is inexistent. According to the

previous analysis, ice growth and sea-level tilt are the most likely factors that affect vertical movement in this area. The growth rate and maximum value of the ice draft in these 3 years were nearly equal, as shown in Figure 4. The sea-level tilt for each acquisition date in 2019 was evidently larger than those for the other two years. For example, the east–west tidal tilt from January to March 2019 was 0.5 cm, while those for the same periods in 2020 and 2021 were only 0.1 cm and 0.2 cm, respectively. We speculate that this phenomenon may have been one of the most important reasons for the vertical deformation of landfast ice in 2019. During the three studied years, the wind was dominated by westerlies, with minimal variation in wind speed. No extreme weather or ocean current events were reported in the study area in 2019–2021. Consequently, the deformation characteristics in the horizontal direction remained relatively immobile. In addition, the random internal motion of landfast ice would also have an influence on the deformation results. This influence was not considered in this work.

6. Conclusions

In the current work, the time-series 2D deformation that comprised the horizontal and vertical directions over the landfast ice area in Cambridge Bay was investigated by using ascending and descending datasets from Sentinel-1A and the multi-dimensional SBAS approach. This work is the first to utilize the multi-dimensional SBAS approach to explore the interannual variations (2019–2021) in landfast ice. We first obtained the LOS deformation of landfast ice from January to April in 2019–2021, and we discovered that the experimental results obtained from the ascending and descending datasets tended to exhibit opposite deformation directions due to differences in their imaging geometries. Then, the time-series 2D deformation could be decomposed from the ascending and descending LOS deformation by introducing a transform model. The derived results revealed that the vertical deformation in the study area was mostly within the interval of $[-65, 23]$ cm, while the horizontal deformation was largely within the range of $[-26, 78]$ cm. The maximum annual deformation rate of landfast ice occurred from early January to the end of March, while the movement remains relatively flat from April to May. Furthermore, the comparison of the results for the three years indicated that the magnitude of the time-series deformation results obtained in 2019 was significantly larger than those in the other two years, particularly in the vertical direction.

With the collected external data, including tides, temperature, ice draft, and wind, the factors that affected deformation were classified into two categories in accordance with the deformation directions. The first category included the influencing factors associated with vertical deformation, such as ice growth, temperature, and sea-level tilt. The second category comprised the inducers acting on the horizontal deformation, such as ocean currents and winds. We concluded that wind and sea-level tilt dominated the variability in the deformation in Cambridge Bay, with the largest contributor to the magnitude anomalies of deformation in 2019 being the differences in sea-level tilt changes.

Overall, this work utilized the SBAS-InSAR method to determine interannual landfast ice deformation, which is particularly important for local populations and organisms in anticipating potential hazard events and providing effective early warnings in real time. In addition, this proved that the multi-temporal InSAR technology possesses the capacity of being introduced into surface deformation monitoring in the cryosphere. This work still has some weaknesses. Firstly, deriving the time-series deformation for a period of more than 5 or 10 years is difficult due to the limited data that are currently available. This issue may be addressed in the future with the launches of more SAR satellites, such as Sentinel-1C, ALOS-3, and Tandem-L. Secondly, the internal variability, such as the dynamics of brine inclusions and ice rheology, was not considered when analyzing the influencing factors. Therefore, we will be involved in using longer time series and multi-source data to conduct research and analyze the deformation patterns from a multidisciplinary perspective in the future.

Appendix A

Table A1. List of collected SAR images.

Acquisition Date	Sensor	Flight Direction	Acquisition Date	Sensor	Flight Direction
20181231	S1A	Descending	20200216	S1B	Ascending
20190104	S1B	Ascending	20200307	S1A	Descending
20190112	S1A	Descending	20200311	S1B	Ascending
20190116	S1B	Ascending	20200331	S1A	Descending
20190124	S1A	Descending	20200404	S1B	Ascending
20190128	S1B	Ascending	20200412	S1A	Descending
20190205	S1A	Descending	20200416	S1B	Ascending
20190209	S1B	Ascending	20210101	S1A	Descending
20190217	S1A	Descending	20210105	S1B	Ascending
20190221	S1B	Ascending	20210113	S1A	Descending
20190301	S1A	Descending	20210117	S1B	Ascending
20190305	S1B	Ascending	20210125	S1A	Descending
20190313	S1A	Descending	20210129	S1B	Ascending
20190317	S1B	Ascending	20210206	S1A	Descending
20190325	S1A	Descending	20210210	S1B	Ascending
20190410	S1B	Ascending	20210218	S1A	Descending
20190406	S1A	Descending	20210222	S1B	Ascending
20190422	S1B	Ascending	20210302	S1A	Descending
20190430	S1A	Descending	20210306	S1B	Ascending
20190504	S1B	Ascending	20210314	S1A	Descending
20200107	S1A	Descending	20210318	S1B	Ascending
20200111	S1B	Ascending	20210326	S1A	Descending
20200119	S1A	Descending	20210330	S1B	Ascending
20200123	S1B	Ascending	20210407	S1A	Descending
20200131	S1A	Descending	20210411	S1B	Ascending
20200204	S1B	Ascending	20210419	S1A	Descending
20200212	S1A	Descending	20210423	S1B	Ascending
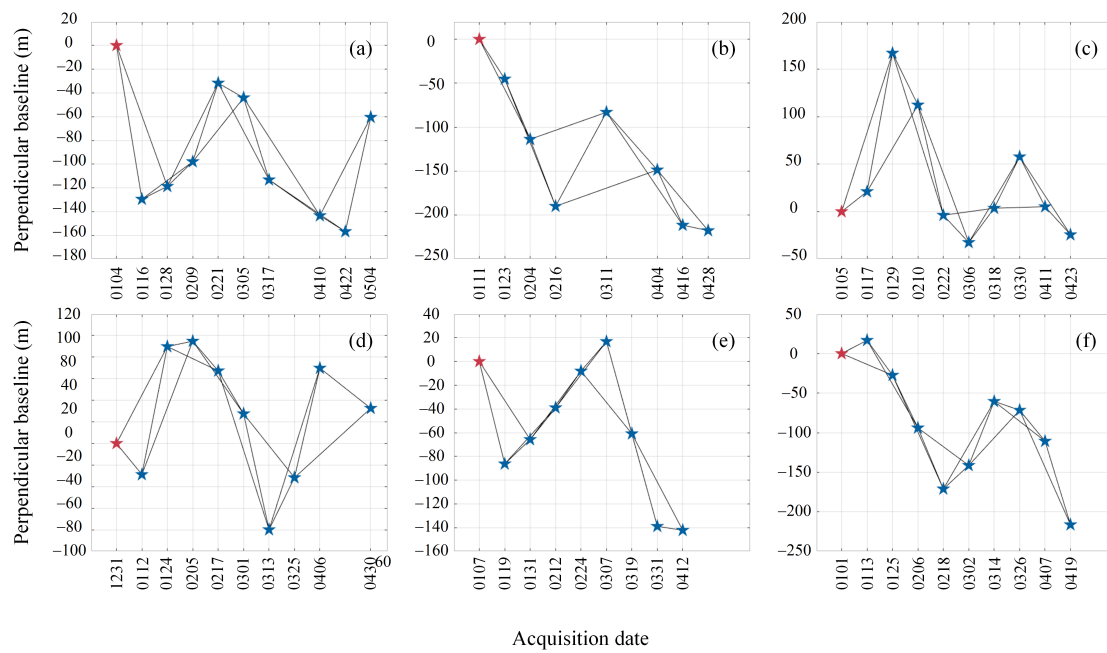
Figure A1. Perpendicular and temporal baselines of selected interferometric pairs. The red star defines the master image, while the blue stars are slave images: (**a**) 2019 ascending, (**b**) 2020 descending, (**c**) 2021 ascending, (**d**) 2019 descending, (**e**) 2020 ascending, and (**f**) 2021 descending.
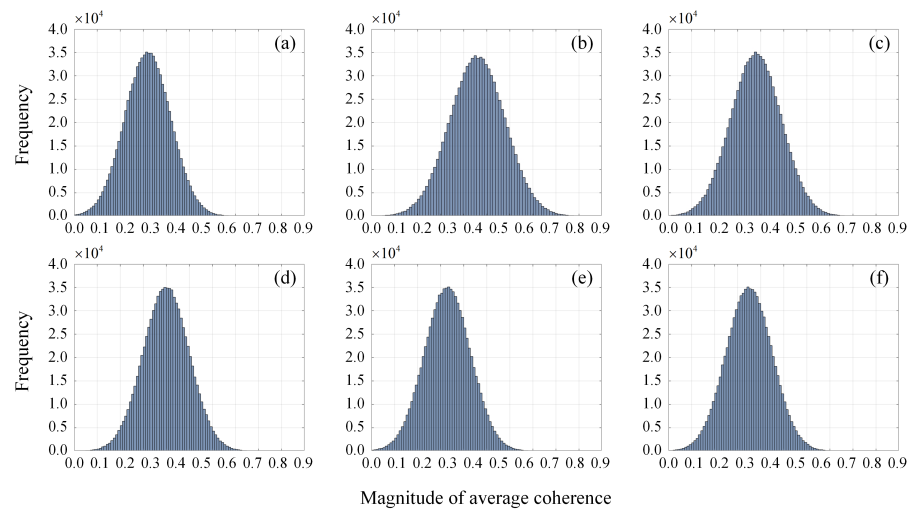
Figure A2. Average coherence histogram: (**a**) 2019 ascending, (**b**) 2020 descending, (**c**) 2021 ascending, (**d**) 2019 descending, (**e**) 2020 ascending, and (**f**) 2021 descending.

Figure A3. Filtered interferograms from ascending [(**a**–**c**): 2019, (**d**–**f**): 2020, and (**g**–**i**): 2021].
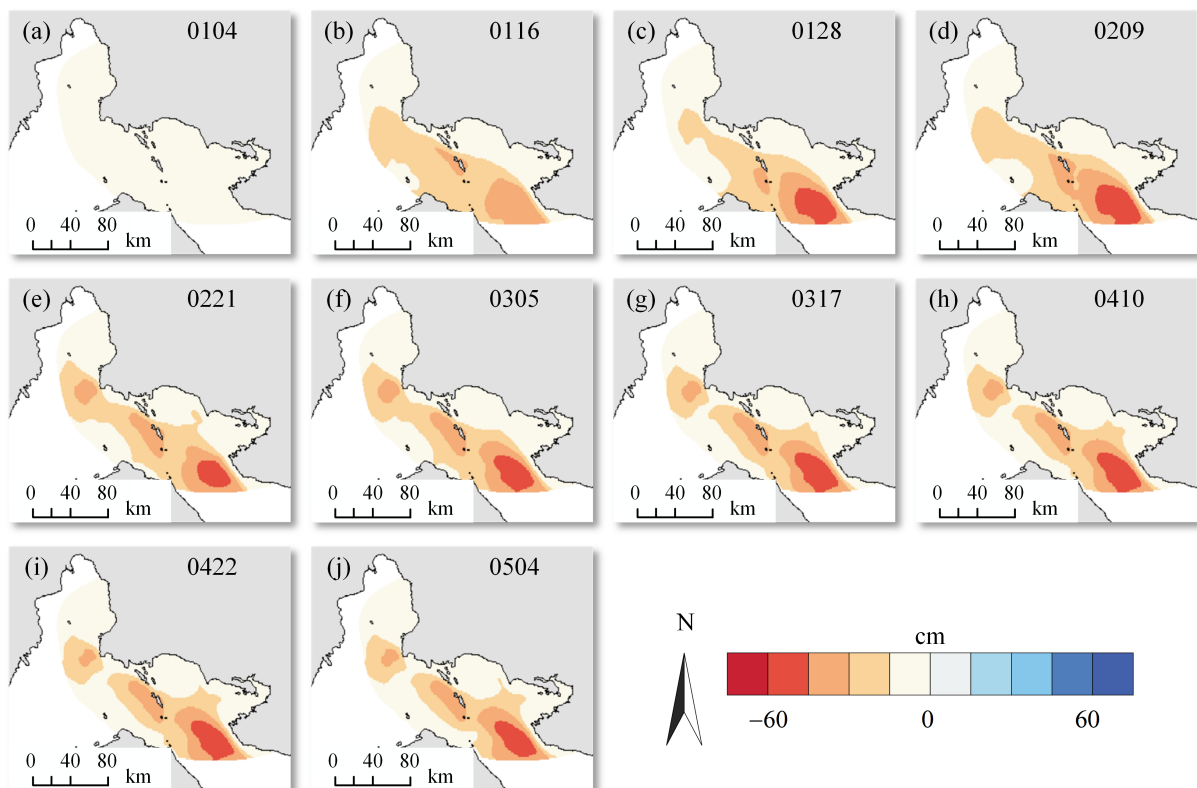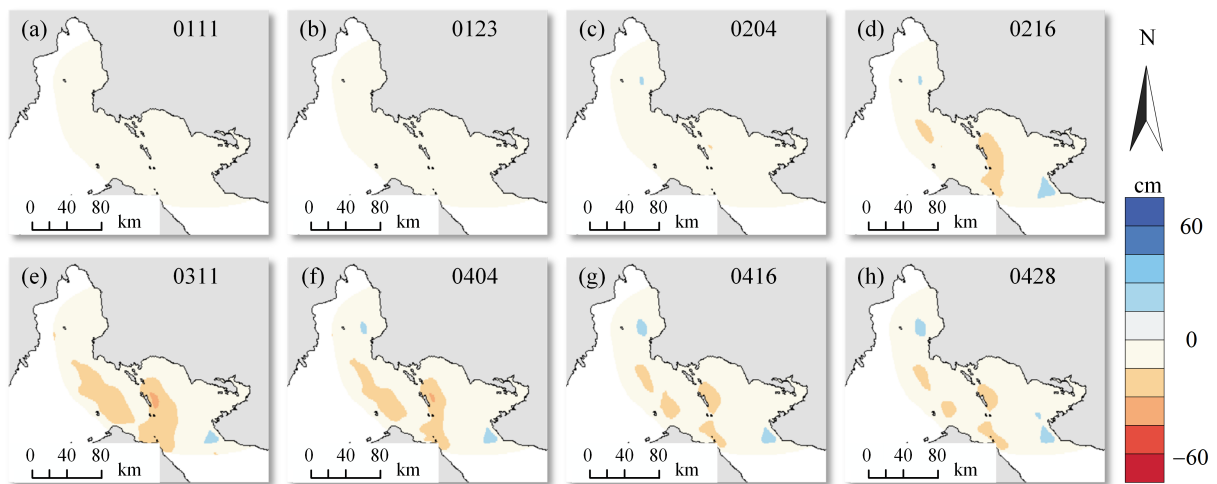

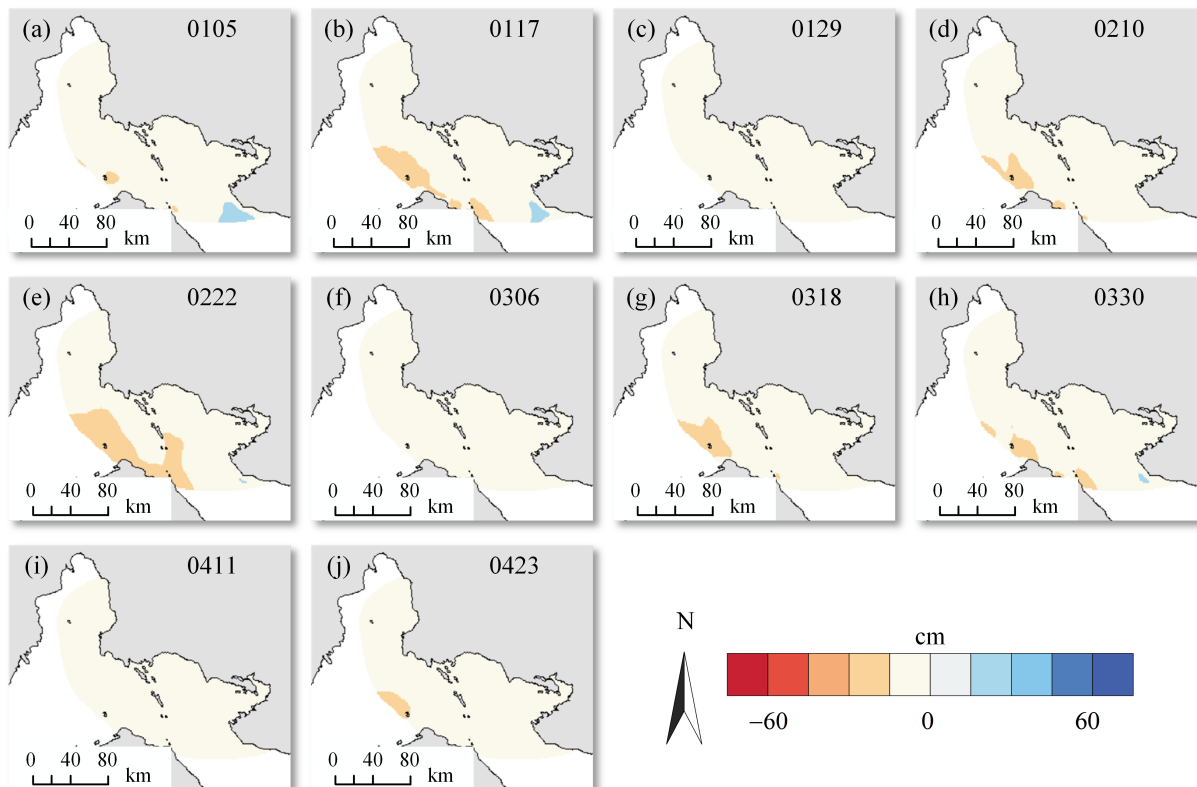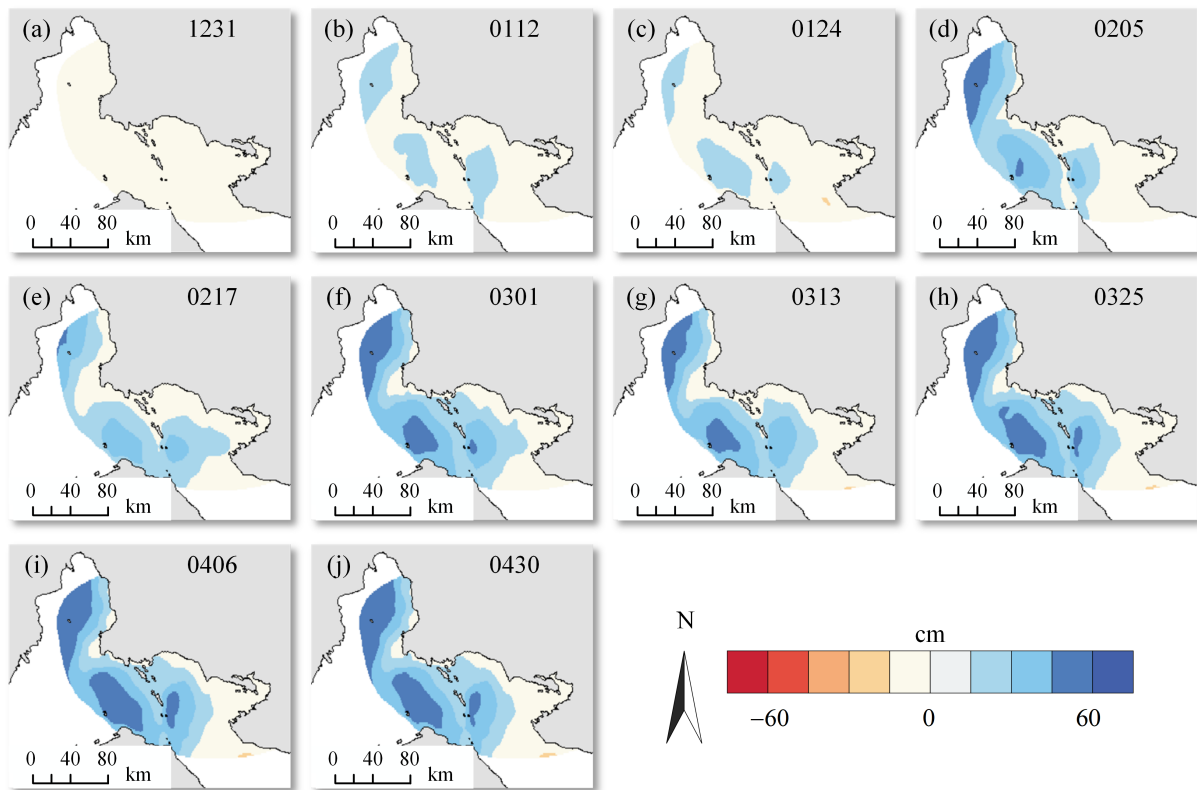**Figure A4.** Time-series LOS deformation retrieved from the 2019 ascending images: the top-right number of subfigures (**a**–**j**) represents the corresponding SAR images acquisition dates.

Figure A5. Time-series LOS deformation retrieved from the 2020 ascending images: the top-right number of subfigures (**a**–**h**) represents the corresponding SAR images acquisition dates.

Figure A6. Time-series LOS deformation retrieved from the 2021 ascending images: the top-right number of subfigures (**a**–**j**) represents the corresponding SAR images acquisition dates.

Figure A7. Time-series LOS deformation retrieved from the 2019 descending images: the top-right number of subfigures (**a–j**) represents the corresponding SAR images acquisition dates.
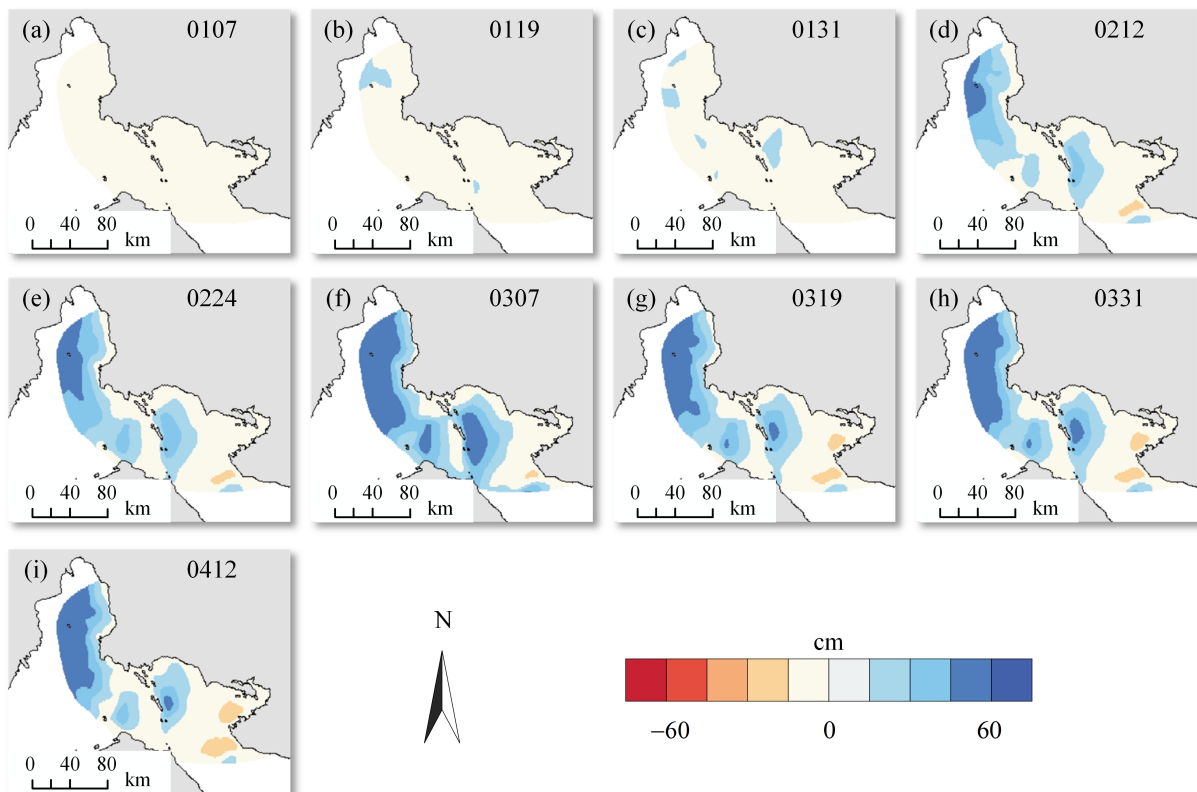

Figure A8. Time-series LOS deformation retrieved from the 2020 descending images: the top-right number of subfigures (**a–i**) represents the corresponding SAR images acquisition dates.
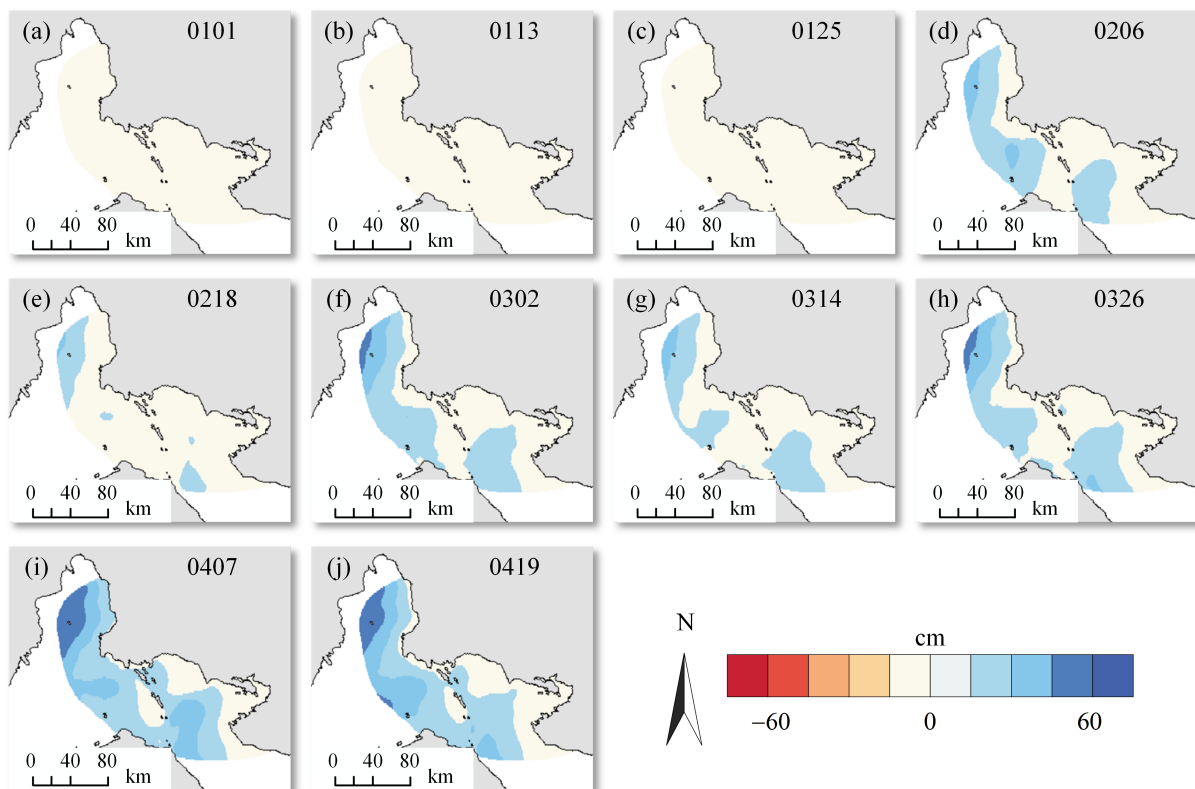
Figure A9. Time-series LOS deformation retrieved from the 2021 descending images: the top-right number of subfigures (**a–j**) represents the corresponding SAR images acquisition dates.

References

1. Laxon, S.W.; Giles, K.A.; Ridout, A.L.; Wingham, D.J.; Willatt, R.; Cullen, R.; Kwok, R.; Schweiger, A.; Zhang, J.; Haas, C.; et al. CryoSat-2 estimates of Arctic sea ice thickness and volume. *Geophys. Res. Lett.* **2013**, *40*, 732–737. [CrossRef]
2. Screen, J.A.; Simmonds, I. The central role of diminishing sea ice in recent Arctic temperature amplification. *Nature* **2010**, *464*, 1334–1337. [CrossRef] [PubMed]
3. Barry, R.; Moritz, R.E.; Rogers, J. The fast ice regimes of the Beaufort and Chukchi Sea coasts, Alaska. *Cold Reg. Sci. Technol.* **1979**, *1*, 129–152. [CrossRef]
4. Howell, S.E.; Laliberté, F.; Kwok, R.; Derksen, C.; King, J. Landfast ice thickness in the Canadian Arctic Archipelago from observations and models. *Cryosphere* **2016**, *10*, 1463–1475. [CrossRef]
5. Yu, Y.; Stern, H.; Fowler, C.; Fetterer, F.; Maslanik, J. Interannual variability of Arctic landfast ice between 1976 and 2007. *J. Clim.* **2014**, *27*, 227–243. [CrossRef]
6. Krupnik, I.; Aporta, C.; Gearheard, S.; Laidler, G.J.; Holm, L.K. *SIKU: Knowing Our Ice*; Springer: Berlin/Heidelberg, Germany, 2010; Volume 595.
7. Eicken, H.; Lovecraft, A.L.; Druckenmiller, M.L. Sea-ice system services: A framework to help identify and meet information needs relevant for Arctic observing networks. *Arctic* **2009**, *62*, 119–136. [CrossRef]
8. Pachauri, R.K.; Allen, M.R.; Barros, V.R.; Broome, J.; Cramer, W.; Christ, R.; Church, J.A.; Clarke, L.; Dahe, Q.; Dasgupta, P.; et al. *Climate Change 2014: Synthesis Report. Contribution of Working Groups I, II and III to the Fifth Assessment Report of the Intergovernmental Panel on Climate Change*; IPCC: Geneva, Switzerland, 2014.
9. Ford, J.D.; Pearce, T.; Gilligan, J.; Smit, B.; Oakes, J. Climate change and hazards associated with ice use in northern Canada. *Arct. Antarct. Alp. Res.* **2008**, *40*, 647–659. [CrossRef]
10. Lovecraft, A.L.; Eicken, H. *North by 2020: Perspectives on Alaska's Changing Social-Ecological Systems*; University of Alaska Press: Fairbanks, AK, USA, 2011.
11. Mesher, D.; Proskin, S.; Madsen, E. Ice road assessment, modeling and management. In Proceedings of the 7th International Conference on Managing Pavements and Other Roadway Assets, Calgary, AI, Canada, 23–28 June 2008.
12. Siitam, L.; Sipelgas, L.; Pärn, O.; Uiboupin, R. Statistical characterization of the sea ice extent during different winter scenarios in the Gulf of Riga (Baltic Sea) using optical remote-sensing imagery. *Int. J. Remote Sens.* **2017**, *38*, 617–638. [CrossRef]
13. Han, Y.; Liu, Y.; Hong, Z.; Zhang, Y.; Yang, S.; Wang, J. Sea ice image classification based on heterogeneous data fusion and deep learning. *Remote Sens.* **2021**, *13*, 592. [CrossRef]

14. Ressel, R.; Frost, A.; Lehner, S. A neural network-based classification for sea ice types on X-band SAR images. *IEEE J. Sel. Top. Appl. Earth Obs. Remote Sens.* **2015**, *8*, 3672–3680. [CrossRef]

15. Li, M.; Zhou, C.; Chen, X.; Liu, Y.; Li, B.; Liu, T. Improvement of the feature tracking and patter matching algorithm for sea ice motion retrieval from SAR and optical imagery. *Int. J. Appl. Earth Obs. Geoinf.* **2022**, *112*, 102908. [CrossRef]

16. Zhang, X.; Dierking, W.; Zhang, J.; Meng, J.; Lang, H. Retrieval of the thickness of undeformed sea ice from simulated C-band compact polarimetric SAR images. *Cryosphere* **2016**, *10*, 1529–1545. [CrossRef]

17. Cooke, C.L.; Scott, K.A. Estimating sea ice concentration from SAR: Training convolutional neural networks with passive microwave data. *IEEE Trans. Geosci. Remote Sens.* **2019**, *57*, 4735–4747. [CrossRef]

18. Fors, A.S.; Brekke, C.; Gerland, S.; Doulgeris, A.P.; Beckers, J.F. Late summer Arctic sea ice surface roughness signatures in C-band SAR data. *IEEE J. Sel. Top. Appl. Earth Obs. Remote Sens.* **2015**, *9*, 1199–1215. [CrossRef]

19. Muhuri, A.; Manickam, S.; Bhattacharya, A.; Snehmani. Snow cover mapping using polarization fraction variation with temporal RADARSAT-2 C-band full-polarimetric SAR data over the Indian Himalayas. *IEEE J. Sel. Top. Appl. Earth Obs. Remote Sens.* **2018**, *11*, 2192–2209. [CrossRef]

20. Qiao, H.; Zhang, P.; Li, Z.; Liu, C. A New Geostationary Satellite-Based Snow Cover Recognition Method for FY-4A AGRI. *IEEE J. Sel. Top. Appl. Earth Obs. Remote Sens.* **2021**, *14*, 11372–11385. [CrossRef]

21. Tsai, Y.L.S.; Dietz, A.; Oppelt, N.; Kuenzer, C. Remote sensing of snow cover using spaceborne SAR: A review. *Remote Sens.* **2019**, *11*, 1456. [CrossRef]

22. Zhang, W.; Zhu, W.; Tian, X.; Zhang, Q.; Zhao, C.; Niu, Y.; Wang, C. Improved DEM reconstruction method based on multibaseline InSAR. *IEEE Geosci. Remote Sens. Lett.* **2021**, *19*, 1–5. [CrossRef]

23. Crosetto, M.; Solari, L.; Mróz, M.; Balasis-Levinsen, J.; Casagli, N.; Frei, M.; Oyen, A.; Moldestad, D.A.; Bateson, L.; Guerrieri, L.; et al. The evolution of wide-area DInSAR: From regional and national services to the European Ground Motion Service. *Remote Sens.* **2020**, *12*, 2043. [CrossRef]

24. Li, S.; Shapiro, L.; Mcnutt, L.; Feffers, A. Application of satellite radar interferometry to the detection of sea ice deformation. *J. Remote Sens. Soc. Jpn.* **1996**, *16*, 153–163.

25. Wang, Z.; Liu, J.; Wang, J.; Wang, L.; Luo, M.; Wang, Z.; Ni, P.; Li, H. Resolving and analyzing landfast ice deformation by InSAR technology combined with Sentinel-1A ascending and descending orbits data. *Sensors* **2020**, *20*, 6561. [CrossRef] [PubMed]

26. Liu, J.; Hu, J.; Li, Z.; Sun, Q.; Ma, Z.; Zhu, J.; Wen, Y. Dynamic estimation of multi-dimensional deformation time series from Insar based on Kalman filter and strain model. *IEEE Trans. Geosci. Remote Sens.* **2021**, *60*, 1–16. [CrossRef]

27. Liu, J.; Hu, J.; Li, Z.; Ma, Z.; Wu, L.; Jiang, W.; Feng, G.; Zhu, J. Complete three-dimensional coseismic displacements due to the 2021 Maduo earthquake in Qinghai Province, China from Sentinel-1 and ALOS-2 SAR images. *Sci. China Earth Sci.* **2022**, *65*, 687–697. [CrossRef]

28. Xing, X.; Chang, H.C.; Chen, L.; Zhang, J.; Yuan, Z.; Shi, Z. Radar interferometry time series to investigate deformation of soft clay subgrade settlement—A case study of Lungui Highway, China. *Remote Sens.* **2019**, *11*, 429. [CrossRef]

29. Berardino, P.; Fornaro, G.; Lanari, R.; Sansosti, E. A new algorithm for surface deformation monitoring based on small baseline differential SAR interferograms. *IEEE Trans. Geosci. Remote Sens.* **2002**, *40*, 2375–2383. [CrossRef]

30. Hu, J.; Li, Z.; Ding, X.; Zhu, J.; Zhang, L.; Sun, Q. 3D coseismic displacement of 2010 Darfield, New Zealand earthquake estimated from multi-aperture InSAR and D-InSAR measurements. *J. Geod.* **2012**, *86*, 1029–1041. [CrossRef]

31. Poland, M.P.; Zebker, H.A. Volcano geodesy using InSAR in 2020: The past and next decades. *Bull. Volcanol.* **2022**, *84*, 27. [CrossRef]

32. Wang, R.; Yang, M.; Dong, J.; Liao, M. Investigating deformation along metro lines in coastal cities considering different structures with InSAR and SBM analyses. *Int. J. Appl. Earth Obs. Geoinf.* **2022**, *115*, 103099. [CrossRef]

33. Wang, Y.; Feng, G.; Li, Z.; Xu, W.; Zhu, J.; He, L.; Xiong, Z.; Qiao, X. Retrieving the displacements of the Hutubi (China) underground gas storage during 2003–2020 from multi-track InSAR. *Remote Sens. Environ.* **2022**, *268*, 112768. [CrossRef]

34. Shugar, D.H.; Jacquemart, M.; Shean, D.; Bhushan, S.; Upadhyay, K.; Sattar, A.; Schwanghart, W.; McBride, S.; De Vries, M.V.W.; Mergili, M.; et al. A massive rock and ice avalanche caused the 2021 disaster at Chamoli, Indian Himalaya. *Science* **2021**, *373*, 300–306. [CrossRef]

35. Zhang, F.; Pang, X.; Lei, R.; Zhai, M.; Zhao, X.; Cai, Q. Arctic sea ice motion change and response to atmospheric forcing between 1979 and 2019. *Int. J. Climatol.* **2022**, *42*, 1854–1876. [CrossRef]

36. Lanari, R.; Casu, F.; Manzo, M.; Lundgren, P. Application of the SBAS-DInSAR technique to fault creep: A case study of the Hayward fault, California. *Remote Sens. Environ.* **2007**, *109*, 20–28. [CrossRef]

37. Arangio, S.; Calò, F.; Di Mauro, M.; Bonano, M.; Marsella, M.; Manunta, M. An application of the SBAS-DInSAR technique for the assessment of structural damage in the city of Rome. *Struct. Infrastruct. Eng.* **2014**, *10*, 1469–1483. [CrossRef]

38. Béjar-Pizarro, M.; Ezquerro, P.; Herrera, G.; Tomás, R.; Guardiola-Albert, C.; Hernández, J.M.R.; Merodo, J.A.F.; Marchamalo, M.; Martínez, R. Mapping groundwater level and aquifer storage variations from InSAR measurements in the Madrid aquifer, Central Spain. *J. Hydrol.* **2017**, *547*, 678–689. [CrossRef]

39. Pritt, M.D. Phase unwrapping by means of multigrid techniques for interferometric SAR. *IEEE Trans. Geosci. Remote Sens.* **1996**, *34*, 728–738. [CrossRef]

40. Strang, G. Orthogonality: projections and least squares approximations. In *Linear Algebra and its Applications*; Harcourt Brace Jovanovich College Publishers: Orlando, USA, 1988; pp. 153–162.

41.   Golub, G.H.; Van Loan, C.F. *Matrix Computations*; JHU Press: Baltimore, MD, USA, 2013.

42.   Zhao, R.; Li, Z.w.; Feng, G.c.; Wang, Q.j.; Hu, J. Monitoring surface deformation over permafrost with an improved SBAS-InSAR algorithm: With emphasis on climatic factors modeling. *Remote Sens. Environ.* **2016**, *184*, 276–287. [CrossRef]

43.   Pepe, A.; Solaro, G.; Calo, F.; Dema, C. A minimum acceleration approach for the retrieval of multiplatform InSAR deformation time series. *IEEE J. Sel. Top. Appl. Earth Obs. Remote Sens.* **2016**, *9*, 3883–3898. [CrossRef]

44.   Fialko, Y.; Simons, M.; Agnew, D. The complete (3-D) surface displacement field in the epicentral area of the 1999 Mw7. 1 Hector Mine earthquake, California, from space geodetic observations. *Geophys. Res. Lett.* **2001**, *28*, 3063–3066. [CrossRef]

45.   Hu, J.; Li, Z.; Zhu, J.; Ren, X.; Ding, X. Inferring three-dimensional surface displacement field by combining SAR interferometric phase and amplitude information of ascending and descending orbits. *Sci. China Earth Sci.* **2010**, *53*, 550–560. [CrossRef]

46.   Huebert, R. Climate change and Canadian sovereignty in the Northwest Passage. In *The Calgary Papers in Military and Strategic Studies*; 2011. Available online: https://cjc-rcc.ucalgary.ca/index.php/cpmss/article/view/36337 (accessed on 22 February 2023).

47.   Tivy, A.; Howell, S.E.; Alt, B.; McCourt, S.; Chagnon, R.; Crocker, G.; Carrieres, T.; Yackel, J.J. Trends and variability in summer sea ice cover in the Canadian Arctic based on the Canadian Ice Service Digital Archive, 1960–2008 and 1968–2008. *J. Geophys. Res. Ocean.* **2011**, *116*, 1–25.

48.   Torres, R.; Snoeij, P.; Geudtner, D.; Bibby, D.; Davidson, M.; Attema, E.; Potin, P.; Rommen, B.; Floury, N.; Brown, M.; et al. GMES Sentinel-1 mission. *Remote Sens. Environ.* **2012**, *120*, 9–24. [CrossRef]

49.   Touzi, R.; Lopes, A.; Bruniquel, J.; Vachon, P.W. Coherence estimation for SAR imagery. *IEEE Trans. Geosci. Remote Sens.* **1999**, *37*, 135–149. [CrossRef]

50.   van der Sanden, J.J.; Short, N.; Drouin, H. InSAR coherence for automated lake ice extent mapping: TanDEM-X bistatic and pursuit monostatic results. *Int. J. Appl. Earth Obs. Geoinf.* **2018**, *73*, 605–615. [CrossRef]

51.   Wang, S.; Lu, X.; Chen, Z.; Zhang, G.; Ma, T.; Jia, P.; Li, B. Evaluating the Feasibility of illegal open-pit mining identification using insar coherence. *Remote Sens.* **2020**, *12*, 367. [CrossRef]

52.   Xing, X.; Zhang, T.; Chen, L.; Yang, Z.; Liu, X.; Peng, W.; Yuan, Z. InSAR Modeling and Deformation Prediction for Salt Solution Mining Using a Novel CT-PIM Function. *Remote Sens.* **2022**, *14*, 842. [CrossRef]

53.   Xing, X.; Zhu, Y.; Xu, W.; Peng, W.; Yuan, Z. Measuring Subsidence Over Soft Clay Highways Using a Novel Time-Series InSAR Deformation Model With an Emphasis on Rheological Properties and Environmental Factors (NREM). *IEEE Trans. Geosci. Remote Sens.* **2022**, *60*, 1–19. [CrossRef]

54.   Dammann, D.O.; Eriksson, L.E.; Mahoney, A.R.; Eicken, H.; Meyer, F.J. Mapping pan-Arctic landfast sea ice stability using<? xmltex\break?> Sentinel-1 interferometry. *Cryosphere* **2019**, *13*, 557–577.

55.   Zhu, Y.; Yao, X.; Yao, L.; Yao, C. Detection and characterization of active landslides with multisource SAR data and remote sensing in western Guizhou, China. *Nat. Hazards* **2022**, *111*, 973–994. [CrossRef]

56.   Xing, X.; Chen, L.; Yuan, Z.; Shi, Z. An improved time-series model considering rheological parameters for surface deformation monitoring of soft clay subgrade. *Sensors* **2019**, *19*, 3073. [CrossRef]

57.   Marbouti, M.; Praks, J.; Antropov, O.; Rinne, E.; Leppäranta, M. A study of landfast ice with Sentinel-1 repeat-pass interferometry over the Baltic Sea. *Remote Sens.* **2017**, *9*, 833. [CrossRef]

58.   Chen, Z.; Montpetit, B.; Banks, S.; White, L.; Behnamian, A.; Duffe, J.; Pasher, J. Insar monitoring of arctic landfast sea ice deformation using l-band alos-2, c-band radarsat-2 and sentinel-1. *Remote Sens.* **2021**, *13*, 4570. [CrossRef]

59.   Chaves-Barquero, L.G.; Luong, K.H.; Mundy, C.; Knapp, C.W.; Hanson, M.L.; Wong, C.S. The release of wastewater contaminants in the Arctic: A case study from Cambridge Bay, Nunavut, Canada. *Environ. Pollut.* **2016**, *218*, 542–550. [CrossRef] [PubMed]

60.   Goldstein, R.V.; Osipenko, N.M.; Leppäranta, M. Relaxation scales and the structure of fractures in the dynamics of sea ice. *Cold Reg. Sci. Technol.* **2009**, *58*, 29–35. [CrossRef]

61.   Rignot, E.; Steffen, K. Channelized bottom melting and stability of floating ice shelves. *Geophys. Res. Lett.* **2008**, *35*, 1–5. [CrossRef]

62.   Berg, A.; Dammert, P.; Eriksson, L.E. X-band interferometric SAR observations of Baltic fast ice. *IEEE Trans. Geosci. Remote Sens.* **2014**, *53*, 1248–1256. [CrossRef]